Application of X-Ray Spectroscopy and Density Functional Theory to Toxicology of Polychlorinated Biphenyls

A Thesis Submitted to the

College of Graduate Studies and Research

in Partial Fulfillment of the Requirements

for the degree of Master of Science

in the Department of Physics and Engineering Physics

University of Saskatchewan

Saskatoon

By

Jay Forrest

PERMISSION TO USE

In presenting this thesis in partial fulfilment of the requirements for a Postgraduate degree from the University of Saskatchewan, I agree that the Libraries of this University may make it freely available for inspection. I further agree that permission for copying of this thesis in any manner, in whole or in part, for scholarly purposes may be granted by the professor or professors who supervised my thesis work or, in their absence, by the Head of the Department or the Dean of the College in which my thesis work was done. It is understood that any copying or publication or use of this thesis or parts thereof for financial gain shall not be allowed without my written permission. It is also understood that due recognition shall be given to me and to the University of Saskatchewan in any scholarly use which may be made of any material in my thesis.

Requests for permission to copy or to make other use of material in this thesis in whole or part should be addressed to:

Head of the Department of Physics and Engineering Physics
University of Saskatchewan
116 Science Place Saskatoon, Saskatchewan S7N 5E2

ABSTRACT

While much is known about the toxicity of polychlorinated biphenyls (PCBs), there are tens of thousands of natural and synthetic chemicals in the environment that can activate the aryl hydrocarbon receptor (AhR) and thus cause toxicity. Since it would be difficult to conduct studies of the toxicity of each and every compound, here is presented a new model based on first-principles taking into account the basic electronic and electron transfer characteristics of PCBs, but can be used to predict the toxicities of other AhR-active compounds. The predictive model is based on Density Functional Theory. The model predicts that the energy gap between highest occupied (HOMO) and lowest unoccupied (LUMO) molecular orbitals is the overarching indicator of toxicity of PCBs, but not the only factor. The model explains why chlorination of both *para*-positions is required for maximum toxic potency. To rank potency of PCBs, the dipole moment in relation to the most chemically active chlorine-sites is critical. The theory is consistent with the accepted toxic equivalency factor (TEF) model for these molecules and is also able to improve on ranking toxic potency of PCBs with similar TEFs. This new model also includes a 13th dioxin-like PCB, PCB 74, not considered in the current TEF model developed by the World Health Organization (WHO). The model was applied to HOMO-LUMO gap measurements of a set of PCBs and the measurements are consistent with the model. Values of HOMO-LUMO gap can also be used to predict bio-accumulation of PCBs. The model provides an *in silico* method to screen a wide range of chemicals to predict their ability to act as an AhR agonist.

ACKNOWLEDGEMENTS

I would like to gratefully acknowledge my supervisor, Dr. Gap Soo Chang, for his teachings and guidance. His unparalleled knowledge and wisdom has made me a better researcher and better man. I would also like to acknowledge particular faculty members of the Physics and Engineering Physics Department. Firstly, Dr. Michael Bradley, whom I could always turn to when facing an electronics problem, and secondly Dr. Glenn Hussey, whom I could turn to when faced with engineering dilemmas.

I would like to dedicate this thesis to my son, Joey, and fiancé, Christie. Without them I would not be able to handle the stresses and strain of life. I know for a fact I would not be in the position I am now if not for Christie. I will always cherish the good times and bad times we spend together. I want to spend the rest of my life paying her back for the support she has given me during my long (and sometimes very stressful) academic career. Seeing Joey laugh and Christie smile makes life easier. I love you very much.

CONTENTS

LIST OF TABLES

LIST OF FIGURES

List of Abbreviations

AhR	Aryl hydrocarbon Receptor
ALS	Advanced Light Source
AO	Atomic Orbital
AR-NEXAFS	Angle Resolved Near Edge X-ray Absorption Fine Structure
BLYP	Becke Lee Yang Parr
CLS	Canadian Light Source
DFT	Density Functional Theory
DM	Dipole Moment
DOS	Density of States
GTO	Gaussian Type Orbitals
HOMO	Highest Occupied Molecular Orbital
HOPG	Highly Ordered Pyrolytic Graphite
IP	Ionization Potential
IPFY	Inverse Partial Fluorescence Yield
LCAO	Linear Combination of Atomic Orbitals
LDA	Local Density Approximation
LUMO	Lowest Unoccupied Molecular Orbital
MO	Molecular Orbital
NEXAFS	Near-Edge X-ray Absorption Fine Structure
NXES	Non-resonant X-ray Emission Spectroscopy
PCB	Polychlorinated Biphenyl
PFY	Partial Fluorescence Yield
PPL	Plasma Physics Laboratory
QSAR	Qualitative Structure-Activity Relationship
RF	Radio Frequency
RIXS	Resonant Inelastic X-ray Scattering
SDD	Silicon Drift Detectror
SGM	Spherical Grating Monochromator
TCDD	2,3,7,8-tetrachlorodibenzo-*p*-dioxin
TEF	Toxic Equivalence Factor
TEQ	Toxic Equivalency
TEY	Total Electron Yield
TF	Thomas Fermi
TFY	Total Fluorescence Yield
UHV	Ultra High Vacuum
WHO	World Health Organization
XAS	X-ray Absorption Spectroscopy
XES	X-ray Emission Spectroscopy

CHAPTER 1

INTRODUCTION

1.1 Motivation

PCBs are a family of man-made toxic molecules once used for many industrial purposes. Their uses range from electrical insulating liquids to sealants. Their main use was for fire retarding liquids in transformers and are still in some today. They are environmentally persistent and have varying human and animal health effects [1]. There has been much work done in determining the toxicity of PCBs. These studies have shown that PCBs are carcinogenic [2], neurotoxic [3], and also affect the endocrine system [4]. PCBs have also been shown to be bio-accumulative [5]. It has been shown that the energy gap between the highest occupied molecular orbital (HOMO) and lowest unoccupied molecular orbital (LUMO) is an indicator of the stability in similar molecules [6]; a higher gap implies a more stable molecule with respect to reactions with bio-matter.

The majority of research into the toxicity of PCBs focuses on assays with actual biomaterial, which can take long periods of time and requires the use of laboratory animals. Other work uses qualitative structure-activity relationship (QSAR) calculations. This method is not always accurate and only uses molecular structure (see Fig. 1.1) to determine toxicity. Here we look at the problem from an entirely new approach from the physical nature of PCBs, namely their electronic characteristics. This allows for a fundamental look at the toxicity of PCBs. The aim is to give a model that will not only work for PCBs, but for other similarly toxic materials as well, both synthetic and natural. A secondary motivation for this project is to look closely at the electronic structure of PCBs using synchrotron radiation in the hopes of seeing a "footprint" of toxicity. Currently, it is postulated that PCBs can become less toxic with fewer and fewer chlorines attached [7]. It is possible that this is not the case, therefore the validity of this claim will be investigated.

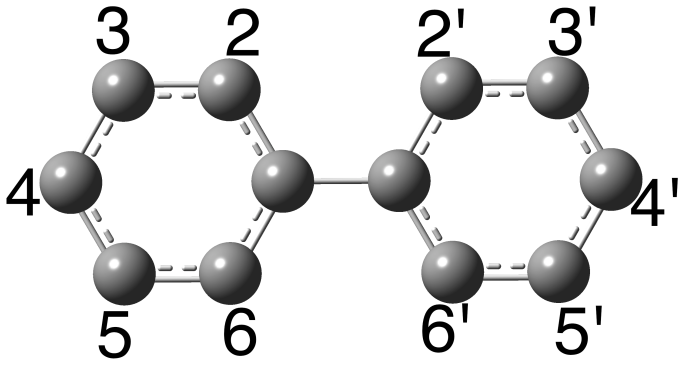

Figure 1.1: PCB molecular structure. The numbers indicate nomenclature used by the field and in this thesis.

The focus of this thesis is on the application of techniques used by material scientists to environmental science, particularly to the toxicity of polychlorinated biphenyls (PCB). A new model to rank the toxicity of PCBs is proposed, based on calculations using density functional theory (DFT) and measurements using synchrotron radiation. This model is the first (to our knowledge) model explaining the toxicity of these molecules and similar molecules using first-principles. The mechanism for interactions between PCBs and bio-matter is not fully understood. The current models for determining toxic effects are statistical, and mainly non-physical. This leaves an opening for a new *strictly* physics model. This new model seeks to find a ranking system based on electron-transfer reactions to and from the PCBs in question. It is understood that certain structural similarities are important in determining the toxicity of individual congeners, which are explained in more basic terms in this thesis.

1.2 Terminology

Due to interdisciplinary nature of this research, the reader may not be versed in the terms understood by someone with a biology or health science background. To remedy this, below are some brief descriptions of toxicological terms used in this thesis.

Dioxin: A dioxin molecule can produce harmful toxicological effects such as carcinogeneity in humans and animals. Dioxin refers to the molecule 2,3,7,8-tetrachlorodibenzo-*p*-dioxin (TCDD), however the definition is sometimes more broad. For our purposes we will use the narrow definition. Other aryl-hydrocarbon receptor (AhR)-mediated molecules, includ-

ing certain PCBs, are dioxin-like. The division between dioxin, dioxin-like and non-dioxin is clearly established by the toxic equivalence factor (TEF) model.

TEF: The TEF model is a ranking system designed to quantify the toxic effects of dioxin and dioxin-like molecules. TCDD has a TEF of 1. All other dioxin-like substances have TEFs on a decreasing logarithmic scale, *i.e.* 1, 0.3, 0.1, 0.03, 0.01, *etc.* The advantage of the TEF model is to calculate the toxicity of mixtures of individual dioxins by a sum of the individual dioxins' TEF multiplied by its concentration, n, resulting in the Toxic Equivalency (TEQ), ie. $TEQ = \sum_{k=1}^{N} n \cdot TEF$.

Bio-Accumulation: A molecule which increases in concentration when moving up the food chain are said to be bio-accumulative. For PCBs and others, this means that they persist in the body, likely in the fat cells of animals.

Carcinogenic: PCBs can damage DNA [2], and damage of this type may result in cancer [8]

AhR: The aryl-hydrocarbon receptor is expected to be the primary receptor of PCBs and other dioxins. It is a molecule within the cell wall that dioxins (and other non-toxic, helpful molecules) bind to, causing a response within the nucleus of the cell. The chemical structure of the receptor is unknown, which makes analysis of interactions very difficult.

QSAR: Historically QSAR was used to calculate boiling points of various molecules. The model uses simple "activity" relationships of molecules to make predictions of other similarly-structured molecules. Activity can be a number of physical properties, such as boiling point, solubility, and toxicological response. This method is also becoming increasingly popular in pharmacology [9]. To improve the model, regression analysis can be performed using experimental data.

Assay: An assay is a laboratory test to determine (in our case) specific toxic responses. The assays performed in the references herein are only performed on laboratory animals and not humans, but human assays are commonplace (medical trials).

CHAPTER 2

THEORY

For the research discussed in this thesis, electronic transfer properties of PCBs are investigated employing synchrotron-radiation X-ray spectroscopy.

Probing the electronic structure of PCB molecules involves the excitation of electrons from core level ($1s$ for carbon) to unoccupied molecular orbitals. To understand the results of the spectroscopic experiments, the following analysis was used.

2.1 Molecular Orbital Theory

Consider a simple example, hydrogen (H), with one electron and a single proton. The wavefunction describing the electron can be calculated analytically and given (in spherical coordinates) by Eq. (2.1).

$$\psi_{nlm}(r,\theta,\phi) = \sqrt{\left(\frac{2}{na_0}\right)^3 \frac{(n-l-1)!}{2n(n+l)!}} e^{-\rho/2} \rho^l L_{n-l-1}^{2l+1}(\rho) \cdot Y_l^m(\theta,\phi) \tag{2.1}$$

where $\rho = \frac{2r}{na_0}$, a_0 is the Bohr radius($\approx 0.53\mathring{A}$), $L_{n-l-1}^{2l+1}(\rho)$ is the generalized Laguerre polynomial, $Y_l^m(\theta,\phi)$ is the spherical harmonic, and n, l, and m are the principle quantum number, angular momentum quantum number, and the magnetic quantum number, respectively.

This normalized wavefunction squared describes the most probable position of the electron in 3-D space (probability density) and by varying the quantum numbers, one can arrive with a series of functions, or atomic orbitals (AO), as seen in Fig. 2.1.

Molecular systems are impossible to calculate analytically, therefore approximations are made to simplify the problem. The approximation used here is known as molecular orbital (MO) theory [10].

Consider a system with two hydrogen atoms separated by a distance R with one H atom positively ionized (missing one electron). The two hydrogens will "bond" or share the remaining electron, provided the atoms are in close proximity, reducing the total energy of the diatomic sys-

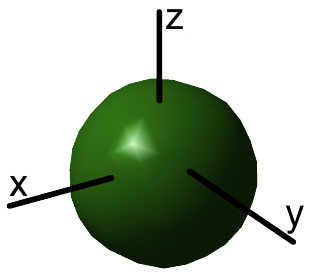

(a) 1s orbital ($n = 1$, $l = 0$, $m = 0$)

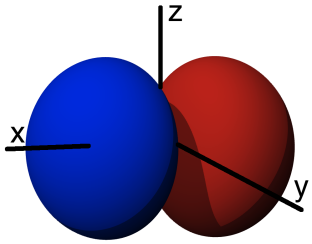

(b) 2p_x orbital ($n = 2$, $l = 1$, $m = \pm 1$)

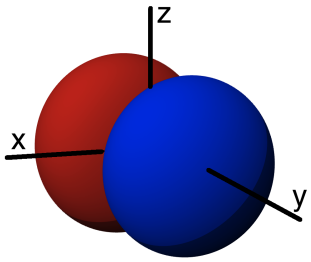

(c) 2p_y orbital ($n = 2$, $l = 1$, $m = \mp 1$)

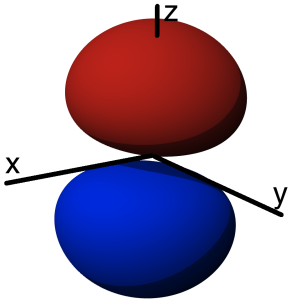

(d) 2p_z orbital ($n = 2$, $l = 1$, $m = 0$)

Figure 2.1: Probability densities of various H-atomic orbitals. Note the radial component of the densities are not shown for clarity.

tem. The electron close to the one H atom, H_A, should have a wavefunction ψ_A and when it is close to the second H atom, H_B, should have a wavefunction ψ_B. Assuming the total wavefunction for the electron is a linear combination of the two separate wavefunctions, the wavefunction of the electron is given by:

$$\psi = c_1\psi_A + c_2\psi_B \tag{2.2}$$

Normalizing ψ results in:

$$1 = N^2\langle(c_1\psi_A + c_2\psi_B) \mid (c_1\psi_A + c_2\psi_B)\rangle \tag{2.3}$$

$$\frac{1}{N^2} = c_1^2\langle\psi_A \mid \psi_a\rangle + c_2^2\langle\psi_B \mid \psi_B\rangle + 2c_1c_2\langle\psi_A \mid \psi_B\rangle \tag{2.4}$$

and if ψ_A and ψ_B are normalized,

$$c_1^2 + c_2^2 + 2c_1c_2S = \frac{1}{N^2} \tag{2.5}$$

where S is known as the overlap integral = $\langle\psi_A \mid \psi_B\rangle$. Then the normalized wavefunction becomes:

$$\psi = \frac{1}{\sqrt{c_1^2 + c_2^2 + 2c_1c_2S}}(c_1\psi_A + c_2\psi_B) \tag{2.6}$$

and the energy of the electron is given by:

$$E = N^2\langle\psi \mid H \mid \psi\rangle \tag{2.7}$$

$$= \frac{\langle(c_1\psi_A + c_2\psi_B) \mid H \mid (c_1\psi_A + c_2\psi_B)\rangle}{c_1^2 + c_2^2 + 2c_1c_2S} \tag{2.8}$$

This is the basis of linear combination of atomic orbitals (LCAO). Multiplying out results in:

$$E = \frac{c_1^2\langle\psi_A \mid H \mid \psi_A\rangle + c_2^2\langle\psi_B \mid H \mid \psi_B\rangle + 2c_1c_2\langle\psi_A \mid H \mid \psi_B\rangle}{c_1^2 + c_2^2 + 2c_1c_2S} \tag{2.9}$$

$$= \frac{c_1^2H_{AA} + c_2^2H_{BB} + 2c_1c_2H_{AB}}{c_1^2 + c_2^2 + 2c_1c_2S} \tag{2.10}$$

where c_1 and c_2 are coefficients for the linear combination and H is the Hamiltonian for the system. Differentiating the electron energy (Eq. 2.10) by c_1 and c_2, so as to minimize the energy gives two simultaneous equations in matrix form:

$$\begin{bmatrix} H_{AA} - E & H_{AB} - E \cdot S \\ H_{BA} - E \cdot S & H_{BB} - E \end{bmatrix} \begin{bmatrix} c_1 \\ c_2 \end{bmatrix} = \begin{bmatrix} 0 \\ 0 \end{bmatrix} \tag{2.11}$$

$$\begin{vmatrix} H_{AA} - E & H_{AB} - E \cdot S \\ H_{BA} - E \cdot S & H_{BB} - E \end{vmatrix} = 0 \tag{2.12}$$

$$(H_{AA} - E) \cdot (H_{BB} - E) - (H_{AB} - E \cdot S)^2 = 0 \tag{2.13}$$

Assuming $H_{AA} = H_{BB}$, *i.e.* homoatomic molecules (both atoms are H), we arrive at 2 solutions:

$$E^+ = \frac{H_{AA} + H_{AB}}{1 + S} \quad \text{and} \quad E^- = \frac{H_{AA} - H_{AB}}{1 - S} \tag{2.14}$$

Given that $0 \leq S \leq 1$ and H_{AB} is negative (shown in Appendix A), one solution in Eq. 2.14 is lower than $H_{AA}(H_{BB})$ (in most cases positive solution) and one higher (most cases negative solution). These are the so-called bonding and anti-bonding solutions or MOs, respectively. The lower energy

MO is then the first to fill with electrons, so as to reduce the total energy. Substituting Eq. 2.14 into Eq. 2.11 results in two solutions:

$$c_2 = -c_1 \quad \text{and} \quad c_2 = c_1 \tag{2.15}$$

The resulting normalized MO wavefunctions are then:

$$\psi_{bonding} = \frac{1}{\sqrt{2+2S}}(\psi_A + \psi_B) \tag{2.16}$$

$$\psi_{anti-bonding} = \frac{1}{\sqrt{2-2S}}(\psi_A - \psi_B) \tag{2.17}$$

These equations assume $A = B$, but that is obviously not always the case. Solving Eq. 2.13 gives (assuming $S \ll 1$ and $H_{BB} \gg H_{AA}$):

$$E_{bonding} \approx H_{AA} - \frac{H_{AB}^2}{H_{BB} - H_{AA}} \tag{2.18}$$

$$E_{anti-bonding} \approx H_{BB} + \frac{H_{AB}^2}{H_{BB} - H_{AA}} \tag{2.19}$$

Thus the energy of the bonding MO is slightly lower than H_{AA} and the anti-bonding MO is slightly higher than H_{BB} (see Fig. 2.2).

This is the established theoretical basis for MO theory, which centers on LCAO. The theory relies on three properties/assumptions, *1*) the atomic orbitals overlap (S) to form MOs when R is small enough, *2*) the individual orbitals ψ_A and ψ_B combine to form bonding (occupied) and anti-bonding (unoccupied) MOs and *3*) the atomic orbitals interact strongly when they have similar energy (H_{BB}-H_{AA} is relatively small, see Eqs. 2.18 and 2.19).

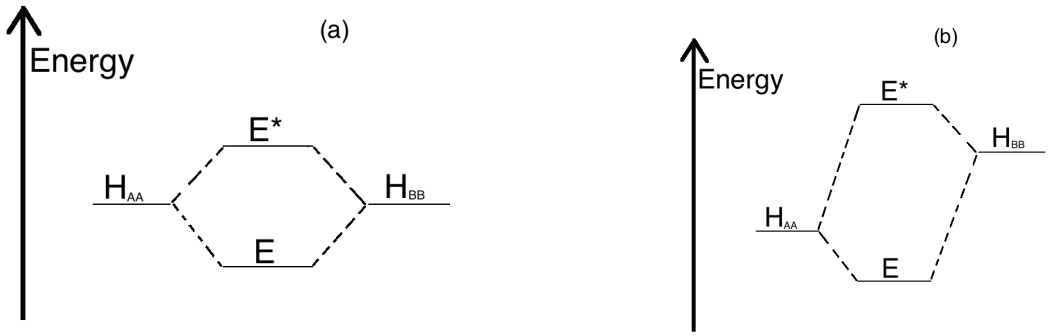

Figure 2.2: Energy level diagrams for bonding and anti-bonding MO for generalized diatomic molecule. (a) When both atoms A and B are the same, (b) Energy levels of MO when A and B are not equal, in this case $H_{AA} \ll H_{BB}$

2.1.1 Symmetry and Overlap of Molecular Orbitals

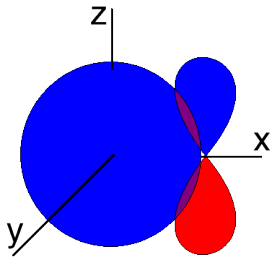

Figure 2.3: Overlap between s and p_z orbitals. The resulting volume integral (purple) is zero.

The focus of this thesis is on low-Z molecules (namely carbon), and in such systems, MOs are classified by their symmetry. These symmetries are known as π and σ orbitals. The differentiatlon is based on the overlap, $S = \langle \psi_A \mid \psi_B \rangle$, defined above. S describes how much one atomic orbital overlaps with another, and as such the bond strength is proportional to it, or conversely it describes how much electron sharing is going on. Not all combinations of atomic orbital overlap actually make bonds because S can be zero even when there is actual overlap. Figure 2.3 shows that the overlap between an s orbital and a p_z orbital will result in a volume integral of 0. Since there is equal overlap (purple) on either side of the x axis, S must be zero. The definition of π and σ molecular orbitals is given by the symmetry of the overlap. When the overlap S is rotationally symmetric about the bond axis, the resulting MO is known as σ. These types come from overlaps

of s - s, s - p_x, s - p_y, p_x - p_x, *etc.*. A π MO forms when the overlap is mirrored above and below the x-y plane. These MO come from p_y - p_y and p_z - p_z overlaps. There is a third type, δ, which is not discussed here but results from double symmetry, a mirror about the x-y plane and a mirror about the x-z plane. The combinations that produce a non-zero overlap for low-Z elements (up to Ca , $Z = 20$) are shown in Fig. 2.4. The examples shown in the figure are all antibonding (* notation). When equal phases overlap (blue-blue, red-red) the result is a bonding orbital. According to Eq. 2.14 of the orbital energy, the energy of a larger overlap (larger S) MO has lower energy (meaning a stronger bond). Since the overlap for π orbitals is less than for σ (see Fig. 2.4) it leads to the energy of π bonds being larger (weaker bond) than σ. Similarly, the energy of π^* orbitals is less than those of σ^*. It is also important to note that the π MO configurations shown in Fig. 2.4(d,e) are rotationally degenerate, which is easily seen from Eq. 2.14.

2.1.2 Hybridization

Certain systems, particularly organic systems, do not follow MO theory as has already been discussed. The bond strengths measured during experiments are not the same as MO theory would predict. Hybridization is a method used to adjust the energies calculated. Hybridization occurs when two atomic orbitals originating from the same atom overlap or "hybridize" to create a new type of AO centered on the atom. An example is $2s$-$2p$ hybridization, as it is the most common and is the only type for the molecules in this thesis.

The resulting wavefunction from a $2s$ atomic orbital hybridizing with a $2p_x$ orbital is:

$$\psi_{hybrid} = C(\psi_{2s} \pm \lambda\psi_{2p_x}) \tag{2.20}$$

where λ is known as the *polarizability* of the atom and C is the normalization constant.

To lower the system energy, the overlap S must be large. An example of a hybridized $2s$-$2p_x$ orbital with $\lambda = 1$ is shown in Fig. 2.5. The asymmetric orbital has a higher energy, but since the overlap is larger the overall energy of the molecule is smaller. A simple example of hybridization is sp^2 *hybridization* which occurs in a benzene ring, shown in Fig. 2.6. All carbon sites are equivalent, *i.e.* each carbon atom bonds to 2 neighbouring carbon atom and one H. There must be 3 equivalent orbitals available for bonding for each site. This is where one $2s$ and two $2p$ ($2p_x$ and $2p_y$) orbitals hybridize, creating 3 $s-p$ hybridized orbitals, hence the name sp^2. These sp^2

orbitals arrange themselves so as to create the largest distance between carbon, *i.e.* 120° apart in a plane. These orbitals leave the $2p_z$ atomic orbital above and below the plane. When the carbon come within bonding proximity, the sp^2 orbitals overlap, creating strong bonds. These bonds have σ symmetry and lie in plane. The remaining $2p_z$ orbitals overlap, forming π MO perpendicular to the plane. Two of the sp^2 orbitals will bond with other sp^2 orbitals and the remaining orbital will bond with a H. There are 4 valence electrons per carbon, so the bonds cannot be all double bonds, nor can they all be single bonds if they need to be equivalent. The new bond type are known as *aromatic* and was first termed by August Wilhelm Hofmann in 1855[11]. This bond is thought of as a superposition of both double bonds and single bonds at alternating sites, resulting in an average of 1.5 electrons per carbon-carbon pair.

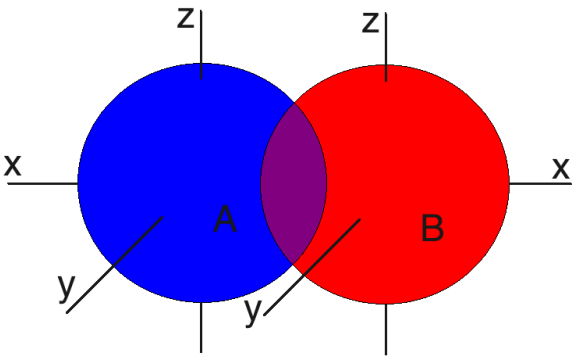

(a) $s - s$ overlap, resulting MO is σ*

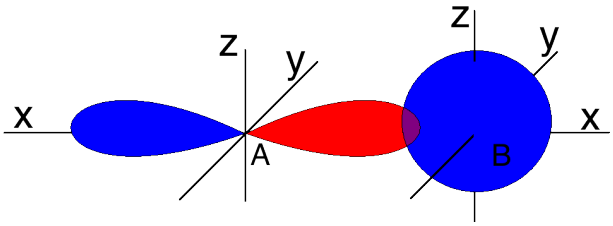

(b) $s - p_x$ overlap, resulting MO is σ*

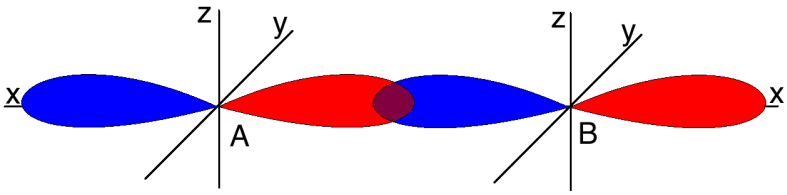

(c) $p_x - p_x$ overlap, result is also σ*

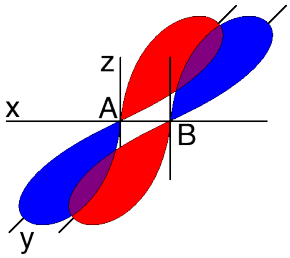

(d) $p_y - p_y$ overlap, resulting is π* symmetry

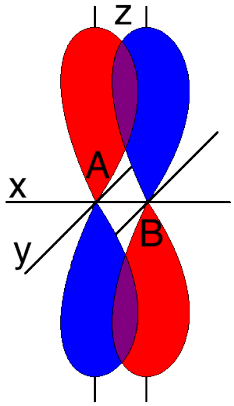

(e) $p_z - p_z$ overlap, resulting is π* symmetry

Figure 2.4: Types of overlap between two atoms, A and B for low-Z elements forming molecules. Purple indicates S overlap integral.

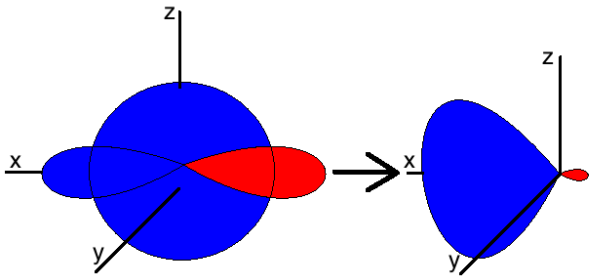

Figure 2.5: $2s$-$2p_x$ hybridized orbital. Note the orbitals are centered on the same atom. The result is an asymetric orbital that when overlapped with a different orbital on another atom will result in a large S, thus stronger bond.

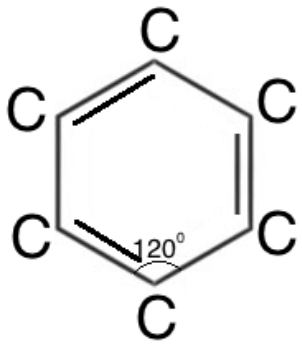

Figure 2.6: Benzene ring molecular structure. The lines between carbon atoms are to show bond angles, not the actual bond structure. Hydrogens atoms are omitted for clarity.

2.2 Density Functional Theory

The difficulty found with MO theory is how to calculate the energies and electron wavefunctions accurately for complex systems. It should be noted that the theory discussed in this section is not the only solution, but it is *a* solution that was used for the work done in this thesis. Discussed are its main points as well as some of its drawbacks.

2.2.1 The *N*-body Problem

In many-electron systems, the Schrödinger equation cannot be solved analytically as the electron-electron interactions make it impossible to separate the differential equation. To remedy this the Thomas-Fermi (TF) model [12, 13] was developed and a more recent implementation was employed by Hohenberg and Kohn [14]. The problem, according to TF, could be solved if the ground state electron density (number of electrons in a specified volume) is known. Hohenberg and Kohn established what is now known as density functional theory. The theory, as the name suggests, treats all measured parameters (energy, dipole moment, *etc.*) as functionals of the electron density.

2.2.2 The Density Functional

As mentioned above, the electrical characteristics can be calculated by finding the proper electron density. The first theorem of DFT is that the external potential, $v(r)$ can be determined by the density, $n(r)$, and each potential is unique to a given density.

Given two potentials, $v(r)$ and $v'(r)$, with ground state wavefunctions $\psi(r)$ and $\psi'(r)$ and energies E and E' which are solutions to their respective Hamiltonians H and H' as shown:

$$E' = \langle \psi' \mid H' \mid \psi' \rangle < \langle \psi \mid H' \mid \psi \rangle = \langle \psi \mid (H + V' - V) \mid \psi \rangle \tag{2.21}$$

$$E' < E + \int [v'(r) - v(r)] n(r) dr \tag{2.22}$$

By interchanging prime and unprime quantities,

$$E < E' + \int [v(r) - v'(r)] n(r) dr \tag{2.23}$$

If we add Eqns. 2.22 and 2.23, we see an impossibility (unless *v'*-*v* = const):

$$E + E' < E + E' \tag{2.24}$$

Thus, the potential and the ground state energy and wavefuntion are unique functionals of the density. This leads to the correct density functional for a given potential. Taking the energy functional of the wavefunction ψ':

$$\varepsilon\left[\psi'\right] \equiv \langle \psi' \mid V \mid \psi' \rangle + \langle \psi' \mid (T+U) \mid \psi' \rangle \tag{2.25}$$

which is minimum at the ground state, ψ. By a variational principle,

$$\varepsilon\left[\psi'\right] = \int v(r) n'(r) dr + F[n'] \quad > \quad \varepsilon[\psi] = \int v(r) n(r) dr + F[n] \tag{2.26}$$

where $F[n] \equiv \langle \psi \mid (T+U) \mid \psi \rangle$ is the functional of the kinetic (T) and interaction (U) energies. This principle (Eq. 2.26) states that the ground state energy, ε, can be calculated by minimization of the functional *F[n]*. For the majority of systems this functional is difficult to find and approximations must be made to calculate it. The theory also lacks the ability to solve the N-body problem, *i.e.* the U and T terms in F[n] exactly.

2.2.3 The Kohn-Sham Equation

According to Kohanoff [15], the kinetic term (T) is calculated from the Laplacian of the one-body density matrix, which is not obviously related to the electron density. The density in the DFT model is local, *i.e.* it does not take shell structure into account directly. The difficulty with kinetic energy is that it is non-local. On the other hand, Kohn and Sham [16] postulate that a system of non-interacting electrons (over-approximation in some cases) can be described by an antisymmetric wavefunction built of one-electron orbitals. The kinetic term is then:

$$T_R = -\frac{\hbar^2}{2m} \sum_{i=1}^{\infty} f_i \langle \phi_i \mid \nabla^2 \mid \phi_i \rangle \tag{2.27}$$

where f_i are the occupation numbers, and ϕ_i are the one-electron atomic orbital wavefunctions.

A non-interacting system can be found such that it will result in the same density as an interacting system. The kinetic energy in Eq. 2.27 is not exact, as no N-body non-interacting systems

actually exist, but the error in that approximation can be reduced by a correlation term discussed in Section 2.2.4.

Assuming the system is non-interacting, the eigenvectors for the Hamiltonian can be expressed in the form of Slater determinants [17] so as to satisfy the Pauli Exclusion Principle

$$\Phi(r) = \frac{1}{\sqrt{N_S!}} SD[\phi_1(r_1)\phi_2(r_2)\cdots\phi_{N_S}(r_{N_S})] \tag{2.28}$$

where the notation SD[$\cdots$] denotes the determinant:

$$\begin{vmatrix} \phi_1(1) & \phi_2(1) & \cdots & \phi_N(1) \\ \phi_1(2) & \phi_2(2) & \cdots & \phi_N(2) \\ \vdots & \vdots & \ddots & \vdots \\ \phi_1(N) & \phi_2(N) & \cdots & \phi_N(N) \end{vmatrix} \tag{2.29}$$

If we take the occupation numbers to be 2 for $i \leq N_S$ and 0 for $i > N_S$ and $N_S = N/2$ (doubly occupied orbitals), the non-interacting kinetic functional $T_R[n]$ can be written as:

$$T_R[n] = -\frac{\hbar^2}{m} \sum_{i=0}^{N_S} \langle \phi_i \mid \nabla^2 \mid \phi_i \rangle \tag{2.30}$$

and the universal density functional, *F[n]*, can be written as:

$$F[n] = T_R[n] + \frac{1}{2} \iint \frac{n(r)n(r')}{|r-r'|} dr dr' + \tilde{E}_{XC}[n] \tag{2.31}$$

where the integral term is known as the *Hartree* term E_H. The exchange-correlation energy term $\tilde{E}_{XC}$ accounts for the kinetic correlation ignored in Eq. 2.30. Finally the Kohn-Sham equation for the energy functional $\varepsilon[n]$ (Eq. 2.26) is given by

$$\varepsilon[n] = T_R[n] + \int v(r)n(r)dr + E_H + \tilde{E}_{XC}[n] \tag{2.32}$$

2.2.4 Correlation and Exchange

2.2.4.1 Local Density Approximation

The philosophy of the local density approximation (LDA) is to approximate the exchange-correlation energy functional, $\tilde{E}_{XC}$ depending on the local values of the density, averaged over the volume, *i.e.*

$$\tilde{E}_{XC}^{LDA}[n] = \frac{1}{2} \int n(r)\tilde{\varepsilon}_{XC}^{LDA}[n(r)]dr \tag{2.33}$$

It is common to separate the exchange and correlation terms, *i.e.* $\tilde{\varepsilon}_{XC}^{LDA}[n] = \varepsilon_X^{LDA}[n] + \tilde{\varepsilon}_C^{LDA}[n]$ where

$$\varepsilon_X^{LDA}[n] = -\frac{0.458}{r_s} \quad \text{in atomic units} \tag{2.34}$$

and

$$\tilde{\varepsilon}_C^{LDA}[n] = \begin{cases} A\ln r_s + B + Cr_s \ln r_s + Dr_s & \mathrm{r}_s \leq 1 \\ \gamma/(1+\beta_1\sqrt{r_s}+\beta_2 r_s) & \mathrm{r}_s > 1. \end{cases} \tag{2.35}$$

The exchange and correlation energies both come from a homogeneous electron gas. The exchange energy is given exactly by Dirac [18] where r_s is the mean interelectronic distance ($= (3/4\pi n)^{1/3}$). The correlation energy term was found using Monte Carlo simulations by Ceperley and Alder [19]. The fitting parameters are presented in Table 2.1. Highly dense systems (core electrons) are not fit

Table 2.1: Fitting Parameters for Eq. 2.35

Parameter	Polarized	Unpolarized
A	0.01555[20]	0.0311[21]
B	-0.0269[20]	-0.048[21]
C[19]	0.0007	-0.002
D[19]	-0.0048	-0.0116
γ[22]	-0.0843	-0.1423
β_1[22]	1.3981	1.0529
β_2[22]	0.2611	0.3334

well by LDA, as it does not cancel the self-interaction which is stronger at the core. An important aspect of LDA is that the bandgap of molecular systems is underestimated.

2.2.4.2 Gradient Expansions

LDA makes a major oversight in some cases by approximating the density as locally homogeneous. A possible solution is to make an expansion using the gradient of the density. This could (in theory) work perfectly, if an infinite number of terms in the expansion are taken.

$$E_{XC}[n] = \int n(r)\, \varepsilon_{XC}[n(r)]\, F_{XC}[n(r), \nabla n(r), \nabla^2 n(r), \ldots] dr \tag{2.36}$$

One particular gradient expansion was used for this research, namely the Becke Lee Yang Parr (BLYP)[23, 24] expansion. Becke [23] proposes an empirical exchange functional that fits well to molecular systems.

$$\varepsilon_X = \varepsilon_X^{LDA}\left(1 - \frac{\beta}{2^{1/3}A_x}\frac{x^2}{1+6\beta x\sinh^{-1}(x)}\right) \tag{2.37}$$

with $x = 2^{1/3} \mid \nabla n(r) \mid / n(r)^{4/3}$, $A_x = (3/4)(3/\pi)^{1/3}$ and $\beta = 0.0042$

To complement this, Lee *et al.* formulated a correlation functional,

$$\varepsilon_C = -\frac{a}{1+d\,n(r)^{-1/3}}\left\{n(r) + b\,n(r)^{-2/3}\left[C_F\,n(r)^{5/3} - 2t_W + \frac{1}{9}\left(t_W + \frac{1}{2}\nabla^2 n(r)\right)\right]e^{-c\,n(r)^{-1/3}}\right\} \tag{2.38}$$

with $C_F = 3/10(3\pi^2)^{2/3}$, $a = 0.04918$, $b = 0.132$, $c = 0.2533$, $d = 0.349$ and

$$t_W = \frac{1}{8}\left(\frac{\mid \nabla n(r) \mid^2}{n(r)} - \nabla^2 n(r)\right) \tag{2.39}$$

The BLYP expansion is a combination of the work of both Becke and Lee *et. al*. As can be seen by Eqs. 2.37 and 2.38, the exchange energy is a first order gradient expansion, while the correlation functional is 2nd order. The reason is because the exchange energy does not require a large expansion, *i.e.* the inhomogeneities are less prominent in the exchange due to its non-locality. They are however much more prominent in the correlation because it is localized. There are other higher order expansions, as well as hybrid formulations for the exchange-correlation energy (bringing Kohn-Sham and Hartree-Fock[1]together), but they were not used for the work in this thesis.

2.2.5 Basis Sets

To solve the problem mathematically we need a representation of the 1-electron orbitals. There are many ways to do this, but since the work in this thesis focuses on molecular systems the discussion will be limited to what is typically done with such systems. The 1-electron orbital, ψ_j, can be described as a linear combination of our basis set, $\mid \phi_\alpha \rangle$, using expansion coefficients $c_{j\alpha}$.

$$\psi_j(r) = \sum_{\alpha=1}^{M} c_{j\alpha}\phi_\alpha(r) \tag{2.40}$$

[1]Hartree-Fock is a simpler calculation procedure to DFT. It builds wavefunctions purely from Slater determinants and accounts for exchange exactly, but not correlation.

The sum runs to M, which is the size of the basis set. It is theoretically possible to solve the problem with a carefully chosen basis set with very few energy-dependent basis functions. However it is not likely one can find a basis set such as this, so we usually choose an energy-*independent* basis set. The Schrödinger equation can be written in matrix notation,

$$\mathbf{Hc} = \Lambda\mathbf{Sc} \tag{2.41}$$

where Λ is the diagonal matrix of eigenvalues (energies of the basis set orbitals), $\mathbf{c}$ is the basis set matrix with elements as the expansion coefficients, $\mathbf{H}$ is the energy-independent Hamiltonian matrix (elements $\mathbf{H}_{\alpha\beta} = \langle\phi_\alpha \mid \tilde{H} \mid \phi_\beta\rangle$) and $\mathbf{S}$ is the overlap matrix $\big($elements $\mathbf{S}_{\alpha\beta} = \langle\phi_\alpha \mid \phi_\beta\rangle\big)$.

A basis set is typically orthogonal (*i.e.* the individual orbitals are orthogonal to each other), but is not always. Non-orthogonal basis sets do have numerical problems, like different subsets of the functions represent the same MO. The basis functions of interest for this thesis are *atom-centered*, or atomic orbitals.

The basis sets in use for the present study are what are known as Gaussian type-orbitals (GTOs). GTOs are widely popular and were first introduced by Boys [25]. The advantage of GTOs is the Hamiltonian and overlap integrals can be performed with ease, even for 4-centered atoms (overlapping 4 separate atomic orbitals). The natural form of a GTO is

$$\psi_{nlm}(\mathbf{r}) = \frac{2(2\alpha_{nl})^{3/4}}{\pi^{1/4}}\sqrt{\frac{2^l}{(2l+1)!!}}\big(\sqrt{2\alpha_{nl}}r\big)^l e^{-\alpha_{nl}r^2}Y_{lm}(\theta,\varphi) \tag{2.42}$$

A convenient representation (for the computer) is to use Cartesian GTOs,

$$\psi_{ijk}(\mathbf{r}) = \chi_i(x)\chi_j(y)\chi_k(z) \tag{2.43}$$

with the transformation equations,

$$\begin{aligned}
\chi_i(x) &= \left(\frac{2\alpha}{\pi}\right)^{1/4}\sqrt{\frac{(4\alpha)^i}{(2i-1)!!}}x^i e^{-\alpha x^2} \\
\chi_j(y) &= \left(\frac{2\alpha}{\pi}\right)^{1/4}\sqrt{\frac{(4\alpha)^j}{(2j-1)!!}}y^j e^{-\alpha y^2} \\
\chi_k(z) &= \left(\frac{2\alpha}{\pi}\right)^{1/4}\sqrt{\frac{(4\alpha)^k}{(2k-1)!!}}z^k e^{-\alpha z^2}.
\end{aligned} \tag{2.44}$$

The downside of Cartesian GTO is as follows. The spherical harmonics (Y_{lm}) have well-defined angular momenta, l. In quantum mechanics, the allowed m values are $-l \cdots + l$. These functions can be constructed using Eqs. 2.43 and 2.44, with $i + j + k = l$. However the number of Cartesian GTOs for a given l is $(l+2)(l+1)/2$, which is more than the number of independent Y_{lm} for $l \geq 2$ (d-orbitals or higher). There are methods for correcting this, but for the organic molecular systems (without transition metals) in this work those methods are not needed.

The size of the basis set is defined in 3 ways. First, the number of basis functions per atomic orbitals is given. These are single-ζ, double-ζ, triple-ζ, *etc.* for 1, 2, 3, *etc.* functions per AO. Second, the functions used from higher, or unoccupied, angular momenta AOs are known as polarization sets. For carbon, a typical polarization set includes d-type functions ($l = 2$). Third, we have diffuse functions. These functions have small exponents added to the set to improve the results for charged molecules.

2.2.6 Calculation Details

DFT calculations for this thesis were performed using Gaussian 03 [26]. All calculations employed the 3-21G basis set. Exchange-correlation functions used the B3LYP auxiliary sets. Other basis sets were used as a check to determine the closest approximation to experiment. The 6-21G basis set was chosen for its use of computational resources and accuracy. Geometry optimizations were performed, then occupied and virtual (unoccupied) MO energy calculations were done in order to determine DOS, electric dipole moment (DM) of the gas-phase molecules, as well as Mulliken charge population analysis and iso-surface visualizations.

2.3 Synchrotron-Radiation and X-Ray Spectroscopy

Synchrotrons provide a powerful way of performing microscopic imaging [27], scattering/difraction [28], and spectroscopic [29] experiments, since synchrotron radiation can be tuned to specific energies (or conversely, frequencies) and is very bright, as evidenced by Table 2.2. For the electronic structure of PCB molecules, we mainly employed X-ray spectroscopic techniques, which require a minimal knowledge in the operation of synchrotrons. Section 2.3.1 will discuss the important features to understand for proper utilization of such facilities, but is *not* a comprehensive theory on

Table 2.2: Brightness of several light sources [30]

Source	Brightness (photons s^{-1} mm^{-2})
Synchrotron Light	10^{19}
Sunlight	10^{13}
Candle	10^{9}
Medical X-Ray	10^{7}

synchrotrons. The techniques themselves will be discussed in much greater detail in Section 2.3.2.

2.3.1 Synchrotron Radiation and Beamlines

A synchrotron consists (typically) of 4 parts, *a*) an electron source and accelerator (usually a linear accelerator or another synchrotron), *b*) a "booster ring" where the electrons are further accelerated using radio frequency (RF) radiation, *c*) a storage ring where the electrons orbit for several hours and either emit light during its travel around the storage ring or enter *d*) a beamline, or more specifically an insertion device.

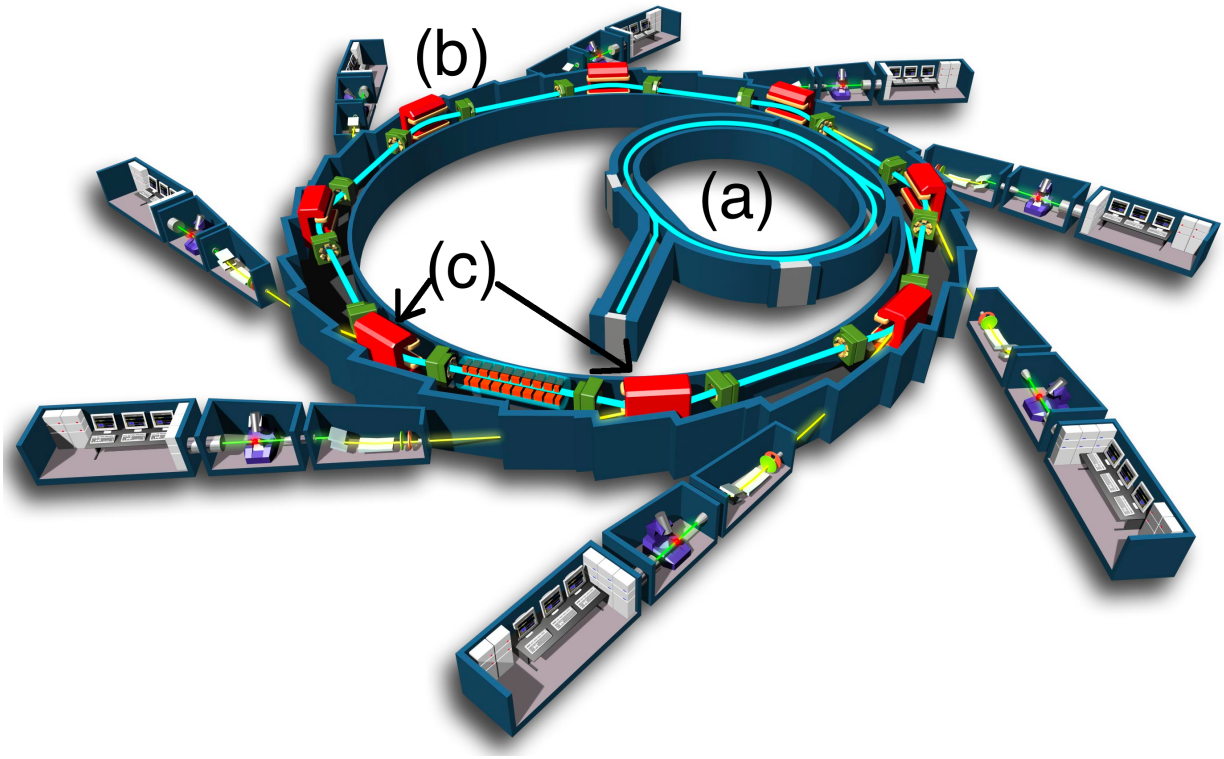

Figure 2.7: Schematic of a synchrotron with (a) booster ring, (b) storage ring and (c) insertion devices. Image taken from [31]

2.3.1.1 Insertion Devices

Insertion devices are the device that creates highly focused, very bright light by modulating the electron motion. There are two main types of insertion devices, bending magnets and undulators. Simplistically, both devices do the same thing; they change the trajectory of electrons such that they emit radiation. The entire theory of synchrotron radiation comes from the Larmor Formula

for relativistic radiation power which can be found in many electromagnetic textbooks [32] [33].

$$P = \frac{e^2}{6\pi\varepsilon_0 c}\gamma^6\left[|\dot{\vec{\beta}}|^2 - |\vec{\beta}\times\dot{\vec{\beta}}|\right] \tag{2.45}$$

with $\vec{\beta}$ and $\dot{\vec{\beta}}$ being the relativistic velocity and acceleration vectors of the electron(s). In the case of synchrotron radiation ($\vec{\beta}\perp\dot{\vec{\beta}}$) Eq. 2.45 simplifies to

$$P = \frac{e^2 c}{6\pi\varepsilon_0}\frac{\gamma^4}{\rho^2} \tag{2.46}$$

with ρ, the radius of the synchrotron. It is clear that if the electrons are *ultrarelativistic* ($\gamma >> 1$) and the radius is small, the output power is huge. There are economic limits to the radius because smaller radii require stronger magnets to bend the electrons. Most synchrotrons have radii on the order of a 100 m, but usually the workhorse (insertion device) has a much smaller radius. Usually the radiation emitted from the electrons travelling the storage ring is unwanted, since the radiation from the insertion device is far better tuned for experiments. The storage ring system typically has to be supercooled since the radiation heats the wall considerably, as well as to ensure the operation of the superconducting magnets.

There are 2 main characteristics of an insertion device, the output light intensity (or power) and the frequency spectrum (or how narrow in energy/frequency can be achieved). The angular and frequency distribution is generally given by [33]:

$$\frac{d^3I}{d\Omega d\omega} = \frac{e^2}{16\pi^3\varepsilon_0 c}\left|\int_{-\infty}^{\infty}\frac{\hat{n}\times\left[(\hat{n}-\vec{\beta})\times\dot{\vec{\beta}}\right]}{(1-\hat{n}\cdot\vec{\beta})^2}e^{i\omega(t-\hat{n}\cdot\vec{r}(t)/c)}dt\right|^2 \tag{2.47}$$

Once the cross-product terms and phase factor are determined from the electrons' trajectory, it is relatively simple to find the frequency and angular spectrum of the synchrotron light for the specific insertion devices.

A bending magnet insertion device works on the same principle as the bending magnets used in the storage ring to keep the electron beam on a circular path. Solving Eq. 2.47 in this case gives:

$$\frac{d^3I}{d\Omega d\omega} = A\left(\frac{2\omega\rho}{3c\gamma^2}\right)(1+x)^2\left[K_{2/3}^2(\xi)+\frac{x}{1+x}K_{1/3}^2(\xi)\right] \tag{2.48}$$

with A absorbing the coefficients from Eq. 2.47, $x=\gamma^2\theta^2$ a simple geometry term (θ is the angle between $\hat{n}$ and x-axis), $K_{1/3}$ and $K_{2/3}$ the modified Bessel Functions of the 2^{nd} kind with argument $\xi = \frac{\rho\omega}{3c\gamma^3}(1+x)^{3/2}$

The Bessel functions severely reduce the output intensity when $\xi \gg 1$. The point where the intensity is highest is with $\xi = \frac{1}{2}, \theta = 0$ is known as the critical frequency. Integrating over the solid angle gives the frequency spectrum

$$\frac{dI}{d\omega} \approx \begin{cases} \frac{e^2}{4\pi\varepsilon_0 c}\left(\frac{\omega\rho}{c}\right)^{1/3} & \omega \ll \omega_c \\ \sqrt{\frac{3\pi}{2}}\frac{e^2}{4\pi\varepsilon_0 c}\gamma\left(\frac{\omega}{\omega_c}\right)e^{-\omega/\omega_c} & \omega \gg \omega_c \end{cases} \tag{2.49}$$

Figure 2.8 shows how the output intensity changes as a function of the output photon energy. This

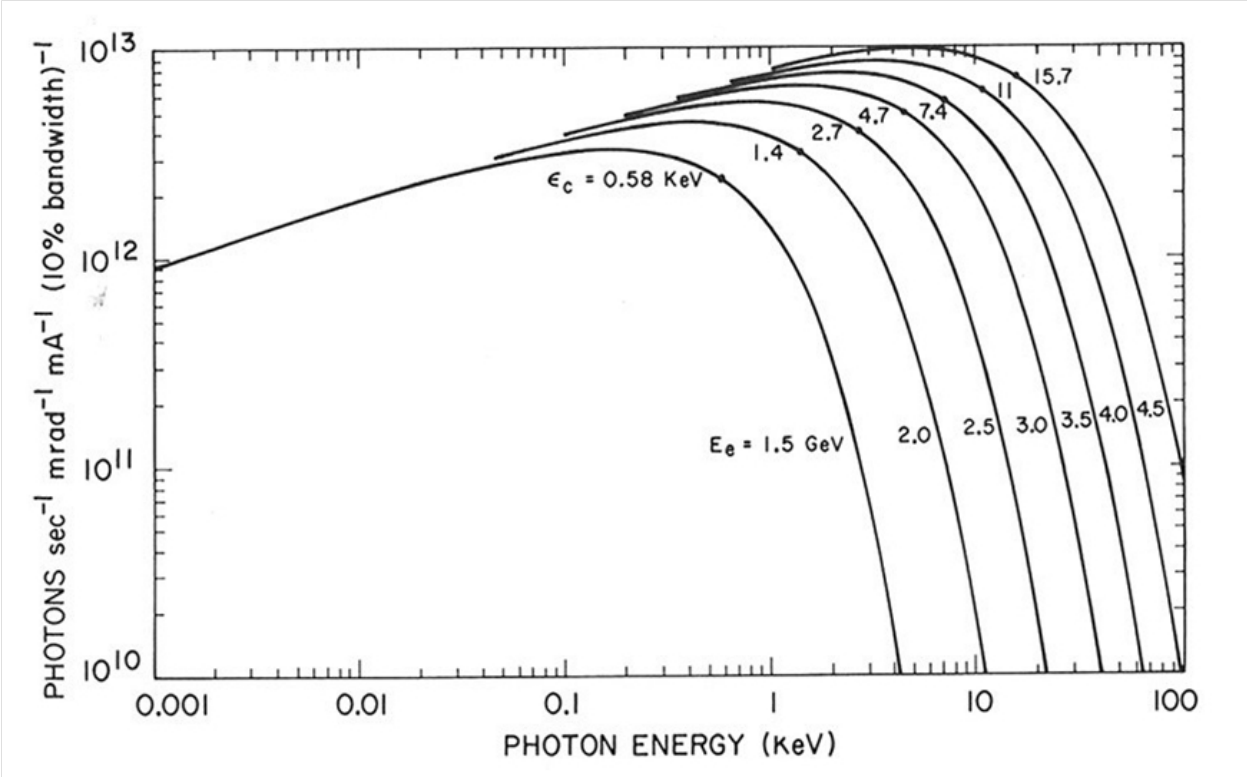

Figure 2.8: Output intensity of a bending magnet as a function of the output photon energy, each line is for a different critical energy (or frequency)[31]

becomes critical when designing the optics for the beamlines, but not overly critical for our uses. It is important to know in any case. More importantly, the two Bessel terms in Eq. 2.48 represent in-plane ($\theta, x = 0$) and out-of-plane ($\theta, x \neq 0$) polarized radiation. Integrating over all frequencies gives a spatial distribution

$$\frac{d^2I}{d\Omega} = \frac{7e^2\gamma^5}{64\pi\varepsilon_0\rho}\frac{1}{(1+x)^{5/2}}\left[1+\frac{5}{7}\frac{x}{1+x}\right] \tag{2.50}$$

Equation 2.50 indicates that the in-plane polarization is the major component, but not the only component. The most important aspect is that the light *is* polarized.

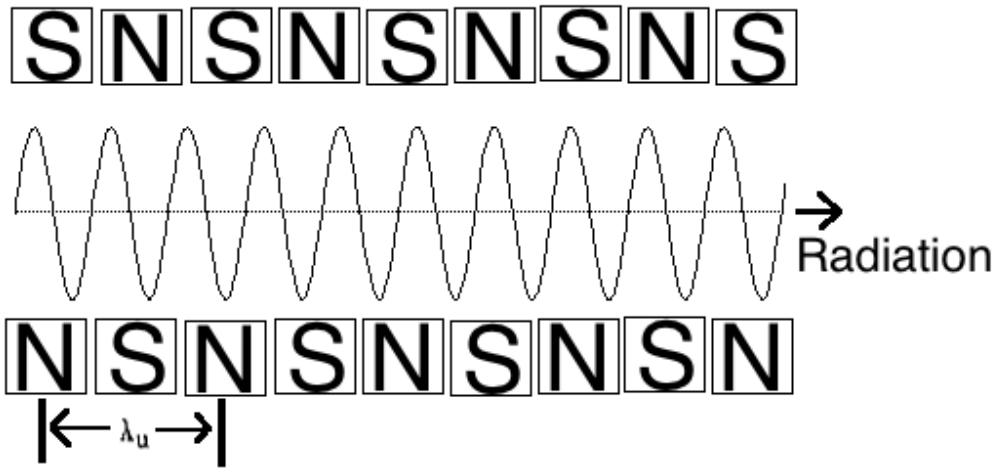

Figure 2.9: Schematic of an undulator, B-field is perpendicular to electron travel and outgoing light

An undulator insertion device has much better spectral resolution than a bending magnet. Undulators consist of an array of alternating magnets, with N-N (or S-S) poles along the same side separated by λ_u (see Fig. 2.9). The magnets produce a sinusoidal magnetic field (amplitude B_0) that causes the electrons to "wiggle" (a common term). There is a very important parameter for an undulator, rightly named the *undulator parameter*, K.

$$K = \frac{eB_0\lambda_u}{2\pi mc} \tag{2.51}$$

The undulator parameter defines the spectral output of the undulator. If $K \gg 1$, the spectral lines are very sharp, giving high resolution. This makes sense, since if λ_u is small, the radiation waves will constructively (and destructively) interfere, causing a very sharp frequency response, similar to a diffraction grating. When $K \ll 1$, the individual waves do not interfere in the same way (above small angle approximation) and the spectral resolution is diminished. In this case the undulator is called a wiggler.

2.3.1.2 Beamline Optics

With the electron beam and insertion device, the outgoing light is still not optimum for experiments; it needs to be monochromatized, focused, filtered and sent to the analysis chamber. Fig-

ure 2.10 is a schematic of the beamline optics for Beamline 8.0.1 at the Advanced Light Source (ALS). The monochromator is a diffraction grating with various geometries, depending on the re-

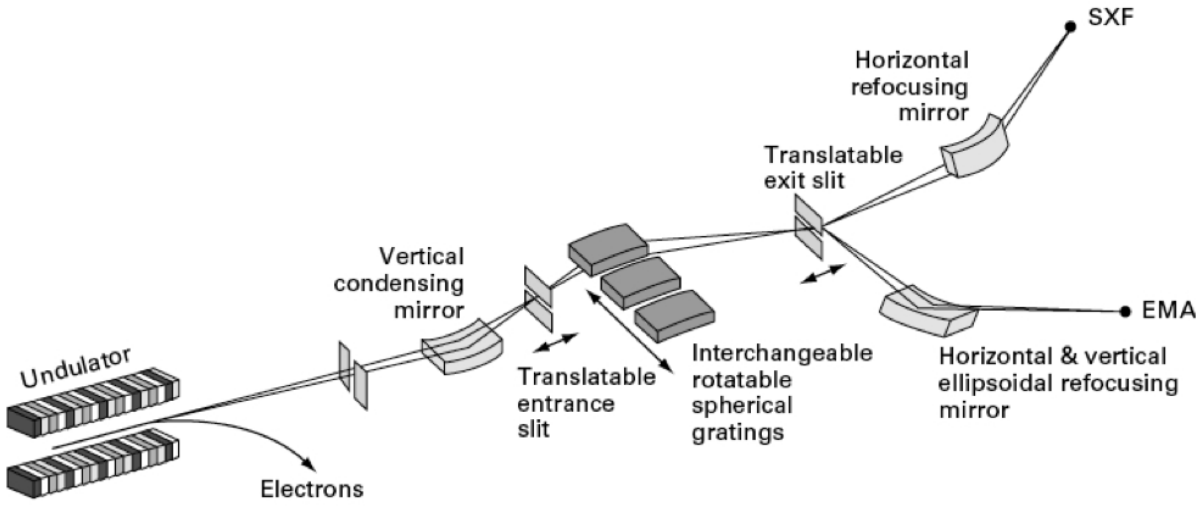

Figure 2.10: Schematic of Beamline 8.0.1 at the Advanced Light Source, Berkely, CA[34]

quirements (in the case of Fig. 2.10, the gratings are spherical). The light being diffracted by the gratings follows Bragg's law, *i.e.* $n\lambda = 2d\sin\theta$. The exit slit is in place to let only the first order light in (or in some cases a different order). The final focusing point of the light is dependent on the energy of light, so careful consideration has to be made for where the samples are placed.

2.3.1.3 Ultra-high Vacuum

There are two components in synchrotrons to consider when it comes to vacuum systems. One is the storage and booster rings. Electrons easily lose energy by atmosphere, even relativistic electrons. To reduce the energy loss, the two rings are under ultra high vacuum (UHV) conditions

(about 10^{-11} torr). The second is in the analysis chamber. Soft X-rays (energy 5-2000 eV) are easily absorbed by low-Z elements such as oxygen, nitrogen and other atmospheric gases. Thus to achieve high enough flux at the sample stage the chamber and all optical components require UHV conditions as well. Hard X-rays are not so easily absorbed therefore do not need vacuum chambers.

2.3.2 X-Ray Spectroscopy

The light from out of an insertion device can be utilized in many ways. In this study, it was used for soft X-ray spectroscopy, namely X-ray absorption spectroscopy (XAS) and X-ray emission spectroscopy (XES). These techniques are used together to probe the partial density of states of a system. XAS and XES measure the unoccupied (anti-bonding) and occupied (bonding) states, respectively. These techniques are similar, in that they both involve the absorption of an X-ray by an electron but the final state of the electron is dependent on the energy of the photon. X-ray spectroscopy techniques are incredibly valuable and powerful for the study of complex molecular (and condensed) systems. Due to their nature, they are element and site specific. This comes from the fact that the synchrotron light has a very small bandwidth (see Sec. 2.3.1.1) thus the transitions occurring are only those of the exact energy of the incoming light and that the binding energies of electrons from a specific element are different than those of a different element. A given measurement will not (to within some other effects) be contaminated by other elements' spectral weight.

Both processes involve the excitation of a core electron by absorption of a photon. Where the electron goes is determined by certain quantum mechanical rules, discussed in Sec. 2.3.2.1. Due to the newly created "core hole" the system is at a higher energy, or excited state. To lower the energy the core hole must be filled. For each technique the core hole is filled by a different electron and will be discussed in further sections. The core hole has the effect of creating a slightly more positively charged nucleus. This pulls the valence electrons closer to the nucleus, thus decreasing the orbital energies. The core hole also has the effect of broadening the features in the measurement. The hole lifetime can be determined in high resolution measurements where the instrumental broadening is negligible. The core hole effect is inherent in the experiment and has its own separate subset of X-ray spectroscopy, but will not be discussed any further in this thesis.

2.3.2.1 Selection Rules

Due to conservation of momentum, not all transitions with energies equal to the incoming photon energy are possible or even probable. This means that the density of states (DOS) picture is not complete with these techniques, but they do give a very good idea. Generally speaking, the selection rules for what transitions can occur are broken into six types, *1*) electric and *2*) magnetic dipole, *3*) electric and *4*) magnetic quadrupole, and *5*) electric and *6*) magnetic octupole. The quadrupole and octupole transitions have extremely low probability since they require secondary processes, therefore the only transition discussed here is the electric dipole. For the purposes of the work in this thesis the only element of interest is carbon. For core level ($1s$) excitations the only electric dipole transition allowable (see Table 2.3) is to the $2p$ ($l = 1$) states. From Section 2.1, those states are π states. So for XAS, the measurements are probing π^* unoccupied states. There are other possible transitions to d and f states (quadrupole and octupole transitions), but these are extremely improbable and those transitions are into unbound states for nonmetal-containing organics.

Table 2.3: Selection rules for electric dipole transitions

Quantum Number	Selection Rule
Δn	only energy constraints
Δl	± 1
ΔS	0
ΔJ	0, ± 1
Δm_j	0,± 1 (exception: only 0 if ΔJ=0)

2.3.2.2 X-Ray Emission Spectroscopy

There are two slightly different techniques in XES, non-resonant X-ray emission spectroscopy and resonant inelastic X-ray Scattering (RIXS). The measurements in this thesis are the elastic kind.

NXES is a photon in-photon out process where the energy of the incoming photon is larger than the energy required to excite a core electron to the occupied or unoccupied states. Since the energy is larger, the electron is released as a photoelectron into unbound (continuum) states. The

core hole is then filled by an electron following the proper selection rules. In the case of C NXES, the only allowable transition is a 2*p* electron from an occupied state. When the 2*p* electron fills the core-hole, a photon is released. The photon energy, $h\nu$, is equal to the difference between the occupied state and the core level. Thus NXES is a probe of the occupied states, relative to the core level binding energy. A simplified schematic of the process is shown in Fig. 2.11. It

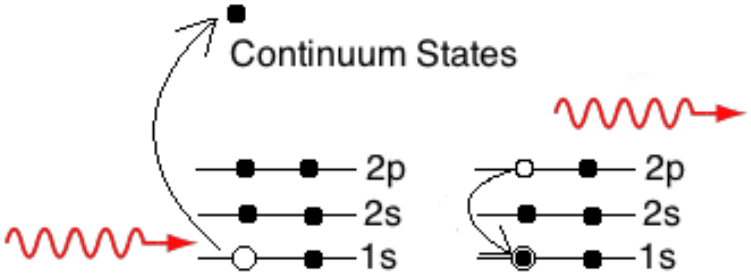

Figure 2.11: Simplified schematic of the NXES process for C. Absorption of a photon by core level electron(left), excited to unbound continuum states followed by filling of the core hole by 2p valence electron and emission of a photon (right)

should be noted here that the probability of a fluorescent transition occurring is extremely low [35], especially for low Z elements. To combat this one of two solutions are possible, *1*) run the experiment for longer time, increased total number of photons in; in some cases the sample may be damaged by the long exposure time. *2*) Open the exit slits so as to allow a high flux which can also damage the sample, but typically the duration of exposure is more critical. The latter solution has its drawbacks including low energy resolution due to the extended slit width. With C measurements this can "smear out" fine structure features making it difficult to observe exact peak positions.

2.3.2.3 X-Ray Absorption Spectroscopy

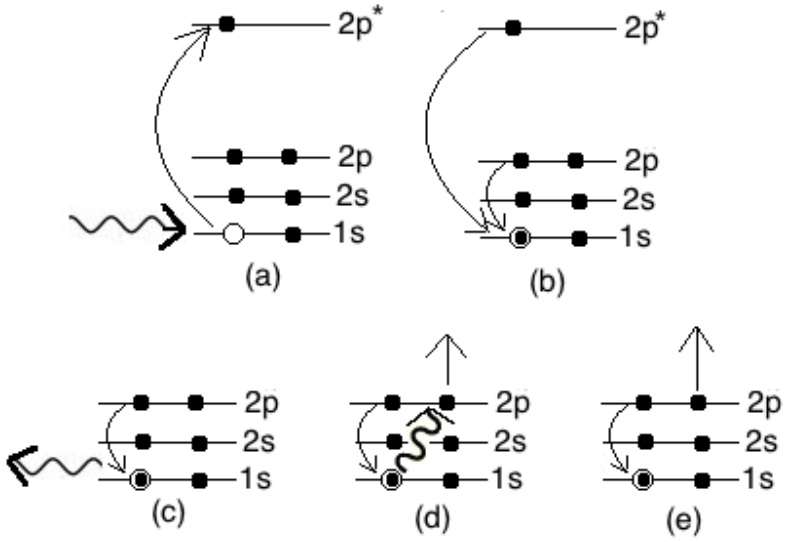

Figure 2.12: A schematic of XAS and its possible detectable quantities. First the absorption of a photon (a) and filling of core hole by either excited or valence electron (b). The first possible outcome is the emission of a photon that can leave the sample (c) or impart energy to a valence electron (d) causing it to leave the sample. The second possibility is the emission of an Auger electron (e).

A technique complementary to XES is XAS, however the process is much more complicated. The process starts the same, *i.e.* an absorption of an X-ray photon creating a core hole, but the energy is such that it excites the electron to bound unoccupied states. The core hole is then filled by either a valence electron or by an excited electron from the unoccupied states. Both cases still must obey the selection rules governing all transitions (see Table 2.3). The filling of the core hole has many possible measurable quantities, each with different probabilities of occurring. The simplest is the emission of a high energy photon which can either leave the sample and be detected or be absorbed by a valence electron (or scattered within the sample and no measurable quantities created). The energy of the photon is much larger (on the order of 100 eV) than the binding energy (work function) of the valence electron thus the electron can leave the sample if it is close enough to the surface. The second possibility is a collisional process between electrons. As the electron decays to fill the core hole it can impart some (or all) of its energy to other valence electrons and those electrons could leave the sample and be detected. This is known as an Auger process. There

are other secondary and tertiary Auger processes which can produce measurable results, but have low probability due to their multi-process nature. A schematic of XAS is shown in Fig. 2.12. As with XES, radiative transitions are less probable in carbon measurements. Thus the typical measurement technique for the experiments discussed in this thesis are of the Auger electrons. However both measurements can be taken simultaneously and in most cases are. The experimental details of both NXES and XAS are discussed in Chap. 3.

CHAPTER 3

EXPERIMENTAL METHODS

Discussed in the following sections are the sample preparation and measurement techniques pertinent to the studies in this thesis. Included are spin coating for sample preparation and X-ray spectroscopic techniques (experimental considerations to Sec. 2.3.2).

3.1 Sample Preparation

One of the most cost-effective methods of creating thin films of soluble materials is using a spin coater shown in Fig. 3.1. The required materials are simply the apparatus, the materials to be spun-coat and the solvents to dissolve the materials in. The spin coater in use is a single wafer unit which operates by securing the substrate of choice to a rotating disc by a venturi-action vacuum and rotating the disc and substrate at a preprogrammed speed while depositing the premixed organic solution onto the substrate. The method will produce a semi-uniform film varying in thickness from 10 nm to 1 μm, depending on the process parameters [36]. The film structure and morphology is usually strongly dependent on the process parameters, but the film structure of the materials for this thesis are not important.

Figure 3.1: Image of spin coater equipment including nitrogen source for venturi vacuum

3.2 TEY and TFY

As discussed in Sec. 2.3.2.3 there are two measurable quantities detected in XAS measurements - photons and Auger electrons. The method of measuring the photons is known as total fluorescence yield (TFY) while the Auger electron measurement is known as total electron yield (TEY). Both methods are simple counting experiments and (in theory) provide the same information but are entirely different practically. Both counts are cross-referenced to the incoming photon energy to give a spectrum of the partial unoccupied density states.

TFY employs a Channeltron fluorescence detector to count the escaped photons. The Channeltron will detect a photon via the electron cascade effect, where a photon will cause an electron to be emitted within the detector which will hit another electron, which will hit another electron, *etc.* until a large enough free electron "avalanche" for a spark to occur, increasing the photon count by one. The detector is equipped with a mesh with a large positive bias so as to prevent electrons from entering the detector. The detector is placed off-axis from the sample as depicted in Fig. 3.2 so as to prevent elastically scattered photons (which contain no DOS information) from reaching the detector. TFY is known as a "bulk-sensitive" method meaning it contains more information from

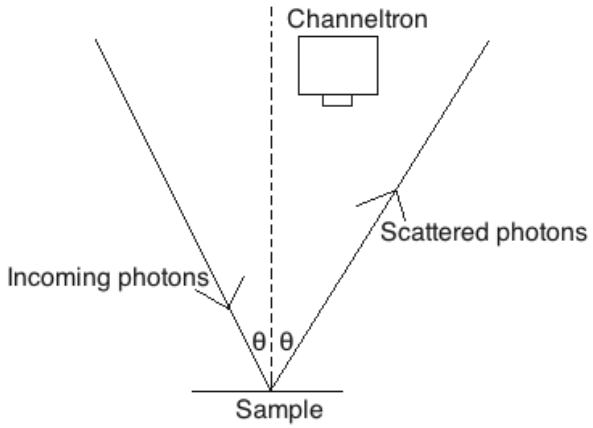

Figure 3.2: Experimental set-up of channeltron detector such that the elastically scattered photons are not detected.

the bulk of the sample and not as much of the surface. This is due to the relatively long mean free path of photons in solids, compared to electrons [37]. As mentioned above, low-Z elements have fluorescence yields significantly lower than the Auger yield, thus it is not used in any pertinent

discussion for this thesis.

TEY is performed using a sample mounting system equipped with an ammeter capable of nA measurements through a connection to ground. When the Auger electron is ejected from the sample the sample is left slightly positively charged. The connection to ground can then "refill" the sample to leave it neutral and the ammeter will measure the total current going to the sample. The current is then a measurement of the number of electrons leaving the sample. TEY is a surface sensitive measurement due to the short mean free path length of electrons. As such, TEY measures the top 2-10 nm of the sample [37].

It should be noted that XAS measurements discussed here do not measure the energy of the escaped photons/electrons; TEY and TFY are simple counting experiments counting at intervals of incoming photon energy. The intensity of either TEY or TFY (number of electrons/photons counted at a specific incoming energy) is not the DOS at that energy, but is merely *proportional* to the DOS at that energy. XAS does however give information on the relative DOS by the relative peak intensities in the measurement.

3.3 Sources of Errors in XAS and Corrections

There are many systematic sources of error in X-ray spectroscopic measurements. Here are the main few with their possible solutions.

3.3.1 Ground versus Excited States

As mentioned above, both NXES and XAS measure not the ground states but the excited states. This is inherent in the measurements, and becomes much more important in higher-Z elements (such as transition metals). For our purposes we can ignore the inconsistent states due to less core hole screening effects. The core hole screening effect comes from the fact that the core (after the core hole is created) is slightly positive. That positive charge draws the inner shells closer but with low-Z elements there are few electrons to pull and the effect is much less. Of course the effect is still there, and as such care must be taken when comparing ground state calculations to excited state measurements.

3.3.2 Energy Calibration and Normalization

There are many components to a synchrotron facility, as discussed in Section 2.3.1. As such there can be many factors that can affect the results of a measurement in some way. One systematic source of error inherent in the experiment is the uncertainty in the energy calibration of the monochromator. The energy of the photons coming from the insertion device to the monochromator cannot be determined directly and there are other uncertainties in the individual components of the beamline such as the diffraction grating, slits, *etc.* which have a measurable effect on the measurements. The optics are calibrated during commissioning and periodically after, but there can never be a precise calibration. Throughout the course of an experiment the calculated energy of the photons can deviate from the actual value - from 0.5 eV to as much as 50 eV in some cases.

To combat this we use calibration samples of highly repeatable spectra and accepted peak locations. This energy calibration should be done whenever it is suspected the optics may have changed. The typical calibration sample for C 1s XAS (and XES) measurements is highly ordered pyrolitic graphite (HOPG). Freshly cleaved HOPG has a sharp π^* resonance at 285.5 eV and sharp π NXES emission feature at 277 eV. By calculating the difference in energy between the measured resonance peak position and the accepted peak position, that difference can be applied to all spectra of similar energy range and same time window (time window is experiment and experimenter dependent). There are some errors introduced by applying a linear shift because the optics are non-linear over a large energy range. Provided the energy scan range is not too large (in our case about 50 eV) the non-linearities do not introduce a significant error. There are some mathematical procedures that could be performed to apply a proper energy calibration in the longer energy scans, but are not performed for the work in this thesis.

The intensity of light (or number of Auger electrons) is supposed to be proportional to the DOS of the sample, however the XAS spectra are systematically subject to variation in the intensity of the incoming X-rays, *i.e.*

$$I \propto (DOS) \cdot I_0 \tag{3.1}$$

where I_0 is the incoming photon flux. If one photon is absorbed and a photon or Auger electron is released, then two absorbed photons would result in two photons or Auger electrons released. If I_0 were constant over the scanned energy range it would not need to be removed, because that

proportionality would have no effect on the shape of the spectra. However that is not the case, so I_0 needs to be removed. What is typically done in soft X-ray beamlines is the placement of a transition metal (gold in our case) mesh that is nearly transparent (to X-rays) after the optics and before the sample chamber. As the X-ray photons hit the mesh most travel through but a few are absorbed by the mesh and a photoelectron is created. That photoelectron is then counted in a similar way to TEY and recorded as an I_0 measurement (in fact, a measurement proportional to I_0). The proportionality in Eq. 3.1 can then be removed by dividing the mesh current out of the spectral intensity and we are left with the intensity proportional only to the DOS. For carbon measurements the experiment get somewhat more complicated. As time goes on for a beamline, the gold mesh can become contaminated with various elements, the worst of which are hydrocarbons. This would not be a problem except that the hydrocarbons have absorption resonances within the energy range of the experiment and in turn create artifacts in the I_0 signal which can be introduced into the measured spectra during normalization. The mesh current is then not a realistic representation of the beam flux reaching the sample. To combat this, the spherical grating monochromator (SGM) beamline personnel have implemented a solution using a photodiode situated behind the sample plate within the experimental chamber directly in the beam path. The photodiode can measure the photon intensity that actually hits the sample. However, in order to take a photodiode measurement the sample must be moved out of the way and the two measurements are not simultaneous. If there are any instantaneous beam instabilities during either the photodiode or XAS measurements this method will not account for it. A sophisticated home-built solution to incorporate both mesh current and photodiode normalization was created, the first step of which is to normalize the measured spectra by the mesh current. The second step is to multiply the normalized spectra by a smoothed (Fast Fourier Transform) mesh current. This will remove any broad artifacts in the mesh current that occur from contamination resonances, but not quick sharp intensity changes due to beam instabilities. The final step is to normalize the resultant spectra by the (usually smoothed to remove noise) photodiode measurement. This procedure has been coded by myself to save time during analysis. Currently there is the option of completely removing the mesh from the path of the beam which has not been tested by myself, but has its advantages particularly with extremely thin samples. To illustrate the differences in normalization procedures, refer to Fig. 3.3. There is not a significant difference in spectra normalized with just the photodiode and with both mesh

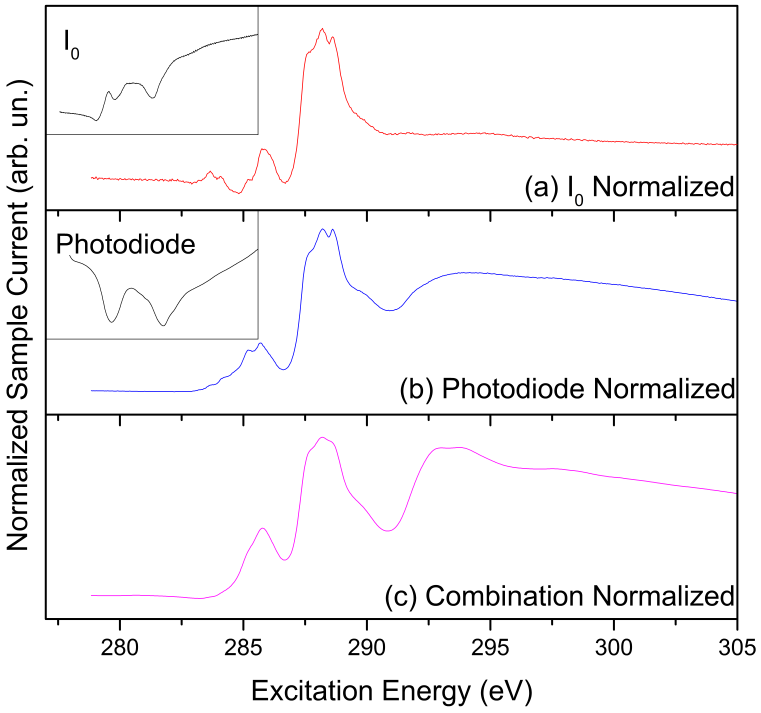

Figure 3.3: The effect of normalization on TIPS pentacene C 1s XAS, note (b) and (c) are similar (some peaks are smoother but only because of different smoothing techniques). The big difference can be seen with purely I_0 normalization. Note insets give normalization spectra.

current and photodiode, but the difference would become apparent if there is an event during a measurement that could distort a final spectra. With the programmed code, the combination normalization can be run on an entire experiment (up to 1000 individual measurements in some cases) within minutes, thus is a better choice.

3.3.3 Radiation Damage

A concern for organic materials is radiation damage during any measurement which involves high intensity light. It has become a quickly growing niche of soft X-ray spectroscopists [38, 39] and can be combated in different ways. A sample can be irradiated with enough flux to create excitations that permanently break bonds.

Due to the spectral distribution of the insertion device, photons of less energy than the tuned energy of interest can be absorbed by the sample and in turn will heat the sample to the point

of outgassing the material, resulting in mass loss. These effects will alter the measured spectra (in some cases significantly) and can cause contamination in the chamber. To reduce the heating, cryo-cooling can be implemented to cool the sample. This solution is not always feasible for the sample or the experiment. The breaking of bonds (and possible creations of others) can severely alter spectral features over the course of a measurement [40]. During an experiment, sequential "radiation damage" scans are performed to indicate if radiation damage is a significant problem for the particular material.

The beamline staff at the SGM have introduced a new method of scanning known as "fast scanning". This method involves the use of fast electronics to sample all required data and move optical components using stepper motors in a pre-defined manner. This allows the user to perform an energy scan in 20s as opposed to typically 15 minutes without it. The fast scanning allows for exposure times to be significantly reduced and radiation damage is minimal. The method also has opened an interesting new realm to studying radiation damage. In some cases the radiation damage can be quick (order of 1 min) and with the slower scan the changes would not be noticeable but the fast scanning allows for much better temporal resolution. Researchers can perform sequential fast scans to watch the damage occur and quantify the damage. One downside of the fast scanning is its infancy. The beamline staff still have non-linearities to calibrate, so the relative error of the energy calibration is increased particularly in the higher energy portion of the scan (σ^* region). When comparing spectra of the same sample from the fast-scan mode to the typical mode, the sigma features will typically appear at lower energies. To help reduce damage in either scan mode the beam spot is moved around the sample.

3.3.4 Self-Absorption

Self absorption is what the name suggests, as a photon exits the sample it could be re-absorbed by the sample if it has the right energy. With carbon measurements the background shape of the spectra comes from oxygen pre-edge (oxygen K-edge is at 540 eV), meaning if we take all the signal from C away from the spectra there will still be a non-zero signal coming from the sample. If the energy of the "background radiation" is the right energy for absorption by the carbon, the background can be seen decreasing, skewing the spectra and broadening features. To detect which photons being counted come from which element, the energy of the photon must be measured. This is done using a silicon drift detector (SDD). The partial fluorescence yield (PFY) can be taken from the SDD for any element of choice (by choosing the energy). By inverting the PFY one can arrive at the inverse partial fluorescence yield (IPFY) which has been shown be a more accurate picture of the DOS [41]. This method works when there are high concentrations of (typically) diatomic molecules such as LiF, NiO and other transition metal oxides but not well for organics due to their low fluorescence. TEY is the best method for organics.

3.4 Experimental Details

PCB materials were obtained from Wellington Laboratories (Guelph, Canada). One set of these were then exposed to a rainbow trout microsome and incubated at 37°C for three hours. The microsome was then extracted, leaving only metabolites of the reaction. Those metabolites were then dissolved in 200 μL hexane. The spin-coated films of the samples were fabricated on Si (100) wafers spun at 800 rpm for 20 seconds, ready for spectroscopic measurements.

All C 1s XAS measurements were taken at the SGM beamline [42] at the Canadian Light Source (CLS), measured in TEY mode. All C Kα NXES measurements were taken at Beamline 8.0.1 of the ALS in Berkley, CA [43] with excitation energy of 310 eV.

CHAPTER 4

RESULTS AND DISCUSSION

4.1 Toxicity Characterization of PCB Molecules

4.1.1 First Principles Model for Toxicity

PCBs consist of two benzene rings bonded at opposite carbon sites, with varying number (1-10) and location of chlorine termination. There are 209 known PCB congeners. The molecular structure of PCBs is shown in Fig. 4.1(a). The situation of the chlorine termination is shown in the figure, indicating nomenclature for the congeners. The most toxic molecules of the PCB family are the so-called "dioxin-like" PCBs. The dioxin-like PCBs are known to activate the AhR. These 12 congeners have a few structural similarities. These similarities are: *1*) they are coplanar, *2*) have either zero or one Cl-substituted ortho position, *3*) have both para positions chlorinated, and *4*) have 2 or more meta positions chlorinated.These similarities cannot be pure coincidence, nor can they be fully explained through any other method than first principles. Lynam et. al. [6] suggested that the HOMO-LUMO gap is an indicator of the stability of a molecule. DFT calculations were taken to determine the HOMO-LUMO gaps numerically for all 209 PCB congeners. Figure 4.2 presents the HOMO-LUMO gap calculated with respect to the torsional angle between two benzene rings (α). It is clear that the coplanar PCBs ($\alpha = 0^{\circ}$) have (on average) lower HOMO-LUMO gaps. Coplanar PCBs are known to be the most toxic [44], and the HOMO-LUMO gap calculations are consistent with this. This also explains similarity 1. The 12 dioxin PCBs are below the line in Fig. 4.2, indicating a threshold HOMO-LUMO gap for the toxicity of these molecules. Also below the threshold is PCB 74. It does not satisfy similarity 4, but does satisfy the others. The model used here includes it as a possible dioxin-like PCB. It should be noted that the spatial distribution of the HOMO and LUMO do not change with toxicity, as indicated in Fig. 4.1 (b-e). PCB 126 has the highest TEF (see Table 4.1), while PCB107 does not have a known TEF and is above the threshold HOMO-LUMO gap. An interesting feature found in Fig. 4.2 is the distribution of the coplanar and

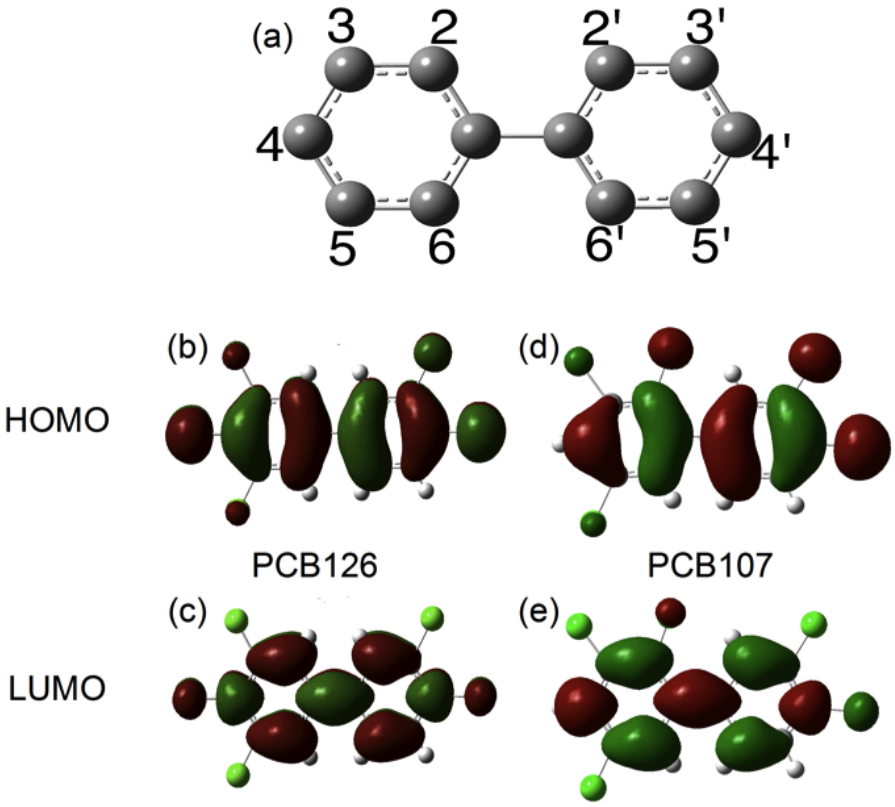

Figure 4.1: (a) Molecular structure of PCBs, para- sites include 4 and 4', meta- sites are 3, 3', 5, and 5', while ortho- sites are 2, 2', 6 and 6. HOMO- and LUMO- isosurfaces of PCB 126 (b and c, respectively) and PCB 107 (d and e, respectively). The spatial distribution of HOMO and LUMO do not change significantly among coplanar PCBs

non-coplanar PCBs. There is little distribution in the HOMO-LUMO gap for the coplanar PCBs (a spread of 0.35 eV for all coplanar and only 0.09 eV for dioxin-like), whereas the spread is wider for the other PCBs (1.2 eV). Since the HOMO-LUMO gap is an indicator of toxicity, a larger spread in the non-coplanar PCBs indicates that the toxicity of the dioxin-like PCBs is in fact a meta-stable state. It would require a small perturbation to cause a large deviation from coplanarity (and in turn increase the HOMO-LUMO gap $\rightarrow$ decrease toxicity), whereas a large perturbation would be required to cause a non-coplanar PCB to become coplanar. If this first-principles method discussed in this thesis is applied to a different set of toxic molecules, a similar analysis can be done, and if the "toxic state" is in fact more stable than the non-toxic, *i.e.* the spread of the HOMO-LUMO gap

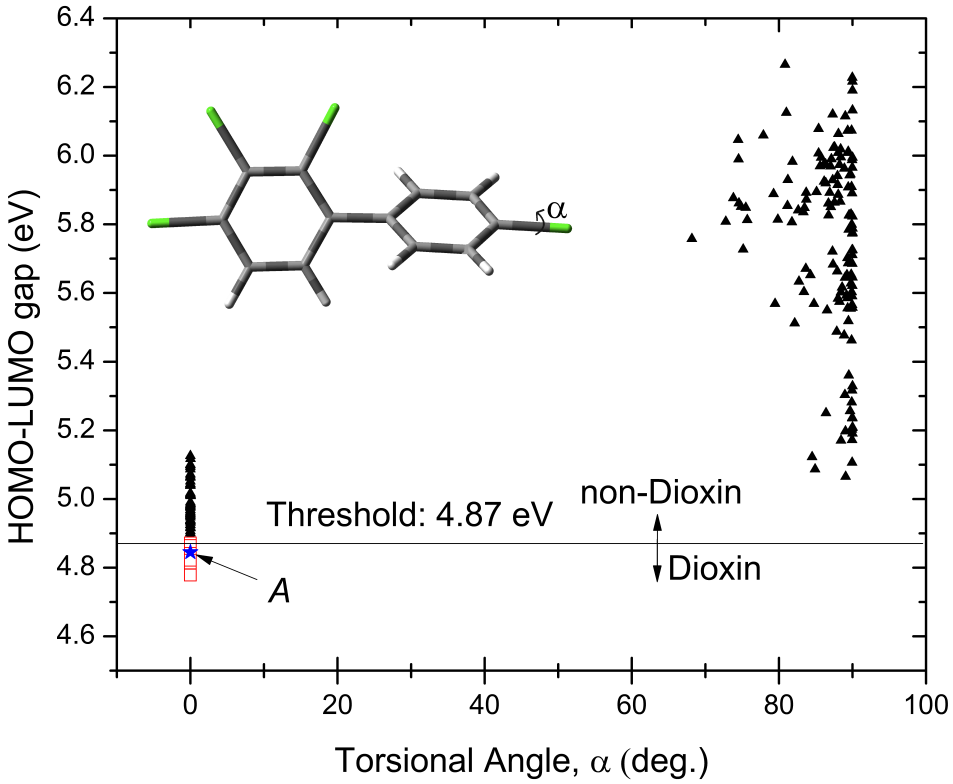

Figure 4.2: Calculated HOMO-LUMO gap of all PCB congeners. Below chosen threshold of 4.87 eV are the 12 dioxin-like PCBs, above threshold are non-dioxins. Note that coplanar PCBs have (on average) lower HOMO-LUMO gaps. PCB 74 ($\star$, A) is considered a possible dioxin, due to its HOMO-LUMO gap below threshold. Torsional angle, α is defined as "twist" around center axis, as depicted in inset.

is broader in the low gap area, it could explain why most congeners of that particular molecule are toxic.

According to DFT, the dioxin-like PCBs have varying HOMO-LUMO gaps (from 4.78 to 4.87 eV). The variation is very small for this type of molecule, and the gaps do not show a trend consistent with the TEF values [44], therefore there must be other factors to consider when relating toxicity in smaller sub-categories. Looking at the Cl-terminated sites of the 12 dioxin-like PCBs we define two terms. These terms explain, quantitatively, what the difference in partial electron charge is for the Cl-terminated sites after ionization. These terms are: Δ_- and Δ_+, for the absolute difference in partial charge of a site between neutral molecule and negatively and positively ion-

ized molecules, respectively. They are a measure of the "activity" of the sites either to accept (-) or donate (+) more electrons. To determine which sites are the most chemically active, a Mulliken charge analysis (part of the Gaussian 03 program) was performed for the dioxin-like congeners. This involved calculating the site partial charge population of the neutral molecule, along with electron-rich (negatively ionized) and electron-deficient (positively ionized) molecules. The ionized molecules were calculated to simulate a state of the molecule during a reaction with another molecule (such as the AhR). It was found that the para positions were most likely to either accept more or donate more of its partial charge when the molecule was ionized, regardless of direction or magnitude of the molecule's dipole moment. This explains similarity 3 above. It should be noted that for PCBs that are coplanar but are missing the para- positions chlorinated, the meta- positions become the most active. This nature of site-specific activity also explains similarity 4. Figure 4.3 shows the average activity of each type (negative and positive ionization) for each site. It is clear that the para sites are the most active, then meta sites followed by ortho sites. The site activity of non-ortho vs. mono-ortho PCBs are also considered to explain the reason non-ortho PCBs are more toxic than mono- or di-ortho molecules. The average activities (both Δ_+ and Δ_-) of all Cl sites of the non-ortho dioxin PCBs are higher than mono-ortho dioxin PCBs. Comparing the average activities of non-ortho PCB with those of mono-ortho PCB (see Fig. 4.3) clearly suggests that the overall activity of the Cl sites is reduced when the ortho position is chlorinated. The averaging also takes away any bias from PCBs with more chlorination, because the average is the average activity for each Cl site. From this, we can conclude that the activity, and in turn the toxicity of mono-ortho PCBs is less than non-ortho PCBs which is consistent with the TEF model. It should be noted that all possible di-ortho congeners are not coplanar, thus are above the dividing line in Fig. 4.2, and as such are not considered dioxin-like. With this, all similarities of dioxin-like PCBs listed above are explained using a first-principles approach.

Chana *et. al.*[45] have previously shown that the magnitude of the DM of the PCB can be an indicator of the selective toxicity of the molecule. Of the 12 dioxin-like PCBs, the DM magnitude varies widely, with no clear trend. Therefore there must be something else governing DM-specific toxicity. The selective toxicity of these dioxin-like PCBs must then come from the *direction* of the DM in relation to the previously discussed site-specific activity. We first look at the 4 most toxic PCBs, PCB126, PCB169, PCB81 and PCB77 in that order. These are the non-ortho PCBs, and due

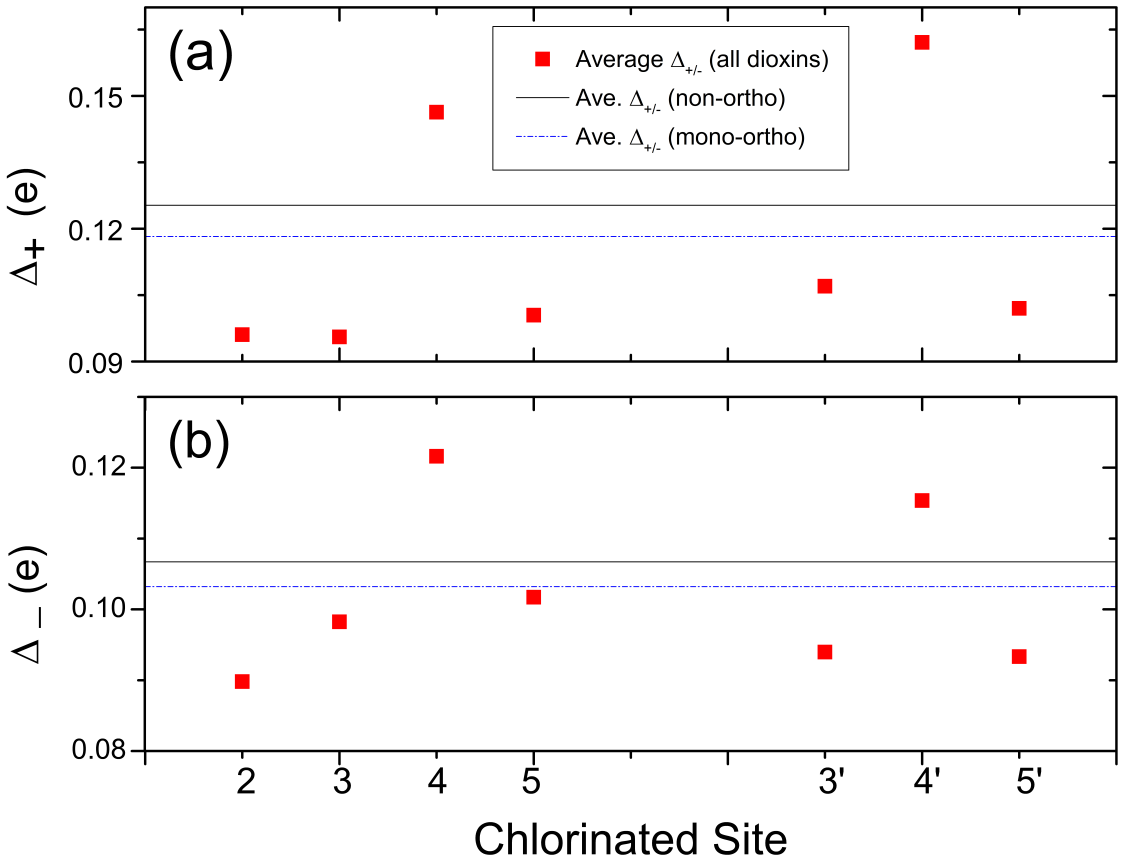

Figure 4.3: Average site-specific activity for (a) giving up electron (b) taking electron for the 12 dioxin-like PCBs. Note the para (4 & 4') sites are most active, then meta (3, 3', 5, 5') then ortho (2, 2'). Also indicated are the average activities of non-ortho and mono-ortho dioxin-like PCBs. In both cases the non-ortho PCBs are more active than mono-ortho.

to the discussion above, are not hindered by the ortho Cl. PCB 126 has a dipole moment directed 61° below the center axis of the molecule, as shown in Fig. 4.4. This DM enhances reactions that may occur at both the meta-3 and the para-4 sites. The high toxicity must then come from the DM direction preferentially choosing the most active sites. PCB 169 is an interesting case, in that its chlorination pattern is symmetric, and as such has no DM but the chlorination pattern is such that all active sites (para and meta) are chlorinated and thus can easily transfer electrons to, or take electrons from a neighbouring receptor. This leads the toxicity to come from random orientations of the molecule, so in turn a lower toxicity than 126, but higher than the others because of its active surface. PCB 81 has a DM directed along the center axis of the PCB. This allows for the molecule

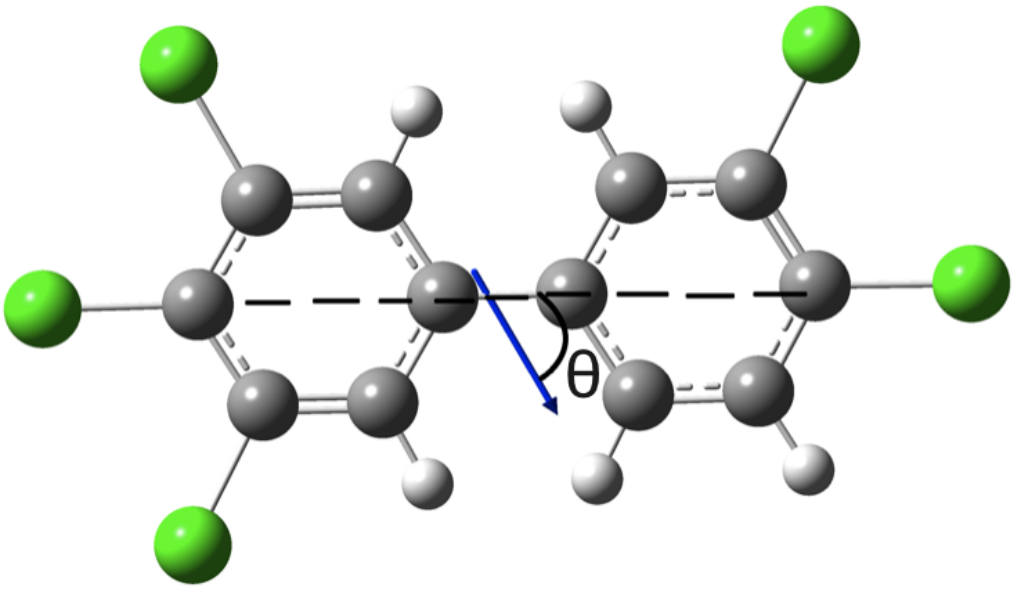

Figure 4.4: PCB 126, showing direction of DM, relative to center axis of molecule (θ). θ is defined as clockwise below center axis, $0^\circ < \theta < 360^\circ$. The DM in this example preferentially allows highly active para- and meta- sites attach to bio-matter.

to align such that it exposes the para- sites. Since these sites have already been established to be the most active, we place PCB 81 in the #3 spot. Finally PCB 77 has a DM directed exactly perpendicular to the center axis. This DM does not preferentially expose the para- sites, however it does expose the meta- sites (both 3 and 3', which are both chlorinated). Due to this DM direction, PCB 77 is placed below the previous 3, but because it is non-ortho it is still higher than the other 8 dioxin-like PCBs. This new first-principles model is established to work for non-otho PCBs, we have ranked the mono-ortho dioxin-like PCBs using the model. There is nothing to compare to (TEF = 0.0003 for all), so there is no known comparative tool. The ranking for all dioxin-like PCBs under our new model is shown in Table 4.1. The trend indicates that DM-center axis angle, θ, causes higher toxicity with $\theta < 90^\circ$, followed by $\theta \sim 120^\circ$. PCB 123 is ranked lower than PCB 189 because the DM does not expose any meta- sites, whereas PCB 189 does. An angle $\theta \sim 90^\circ$ is least toxic, due to not exposing para sites. We also include PCB74 in the list, ranked 13th overall,

lowest due to its mono-meta nature.

Table 4.1: First-principles model ranking of the dioxin-like PCBs. *DM-center axis angle defined in Fig. 4.4.

Rank	**PCB**	**# ortho**	**DM-center axis angle, (θ)***	**TEF**[44]	**# meta**
1	126	0	61.4	0.1	3
2	169		N/A	0.03	4
3	81		0	0.01	2
4	77		90	0.003	2
5	114	1	37.5	0.0003	2
6	118		117		2
7	157		121.3		3
8	189		135.7		4
9	123		120.8		2
10	167		185.9		3
11	105		98.8		2
12	156		91.4		3
13	74	1	336.7	N/A	1

4.1.2 Bioaccumulation of PCBs

Finally, the unoccupied and occupied orbital states were investigated by XAS and XES, respectively and the HOMO-LUMO gaps were determined by superposing the 2^{nd} derivatives of XAS and XES spectra [46]. To determine center peak locations in the spectra, troughs in the 2^{nd} derivative indicate peaks in measured spectra. For molecular systems, the peak center is what indicates the position of the state. The X-ray spectroscopy study focuses on six PCBs molecules: PCB101, PCB105, PCB118 and HCB153. Figure 4.5(a) shows the superposition of C Kα NXES and C 1s XAS measurements of PCB118 (exposed to microsome). Figure 4.5(b) shows the second derivatives of the spectra to determine the HOMO (π) at 281.94 eV and the LUMO (π*) at 285.05 eV.

The same method is used to determine the HOMO and LUMO levels for all of the PCB samples, exposed and unexposed. The results are shown in Fig. 4.6. It is clear to see the trend that the

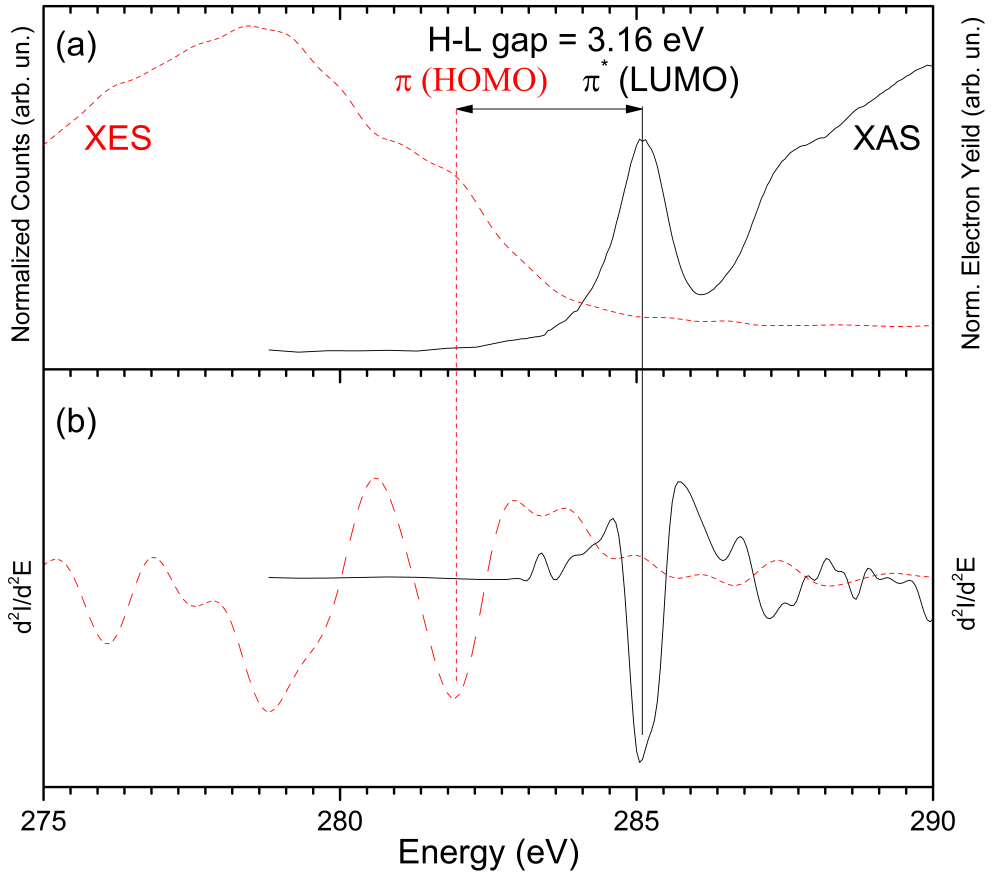

Figure 4.5: (a) Superposition of C Kα NXES and C 1s XAS spectra of PCB 118 (exposed) (b) 2^{nd} Derivative Method to determine HOMO-LUMO gap. HOMO-LUMO gap is determined by difference between π and π* energies, in this case 3.178 eV.

HOMO-LUMO gap increases after exposure. This would imply that the PCBs become more stable after exposure. The relative change of the HOMO-LUMO gap however is different for each PCB. PCB101 has a relative change of 28%, whereas PCB118 has a relative change of only 9%. This change can be an indicator of the bio-accumulitive nature of the PCB. With what we established in Section 4.1.1, in that the HOMO-LUMO gap is the overarching determination of toxicity, then if after exposure the HOMO-LUMO gap changes less for one PCB than the others, that particular metabolite could still be relatively toxic. Here we see the lower relative change (PCB118) PCB would be more bio-accumulative than the others, such as PCB 101.

The HOMO-LUMO gaps measured using this method do not match the calculated values using DFT, but we do not expect them to, as there are intramolecular considerations not taken into account in the DFT calculations as well as inaccuracies in the 2nd derivative method. The DFT method used underestimates HOMO-LUMO gaps of this type of molecule [15] as well. The deviation of calculated HOMO-LUMO gap from measured is $\sim$1.8 eV for the PCBs in this study. We apply a shift of -1.8 eV to the threshold gap in Fig. 4.1 and indicate it in Fig. 4.6. The *trend* is consistent with DFT results, *i.e.* PCBs 105 and 118 (dioxin-like) have a lower HOMO-LUMO gap than the threshold of 2.98 eV, and the other non-dioxin-like are above the threshold.

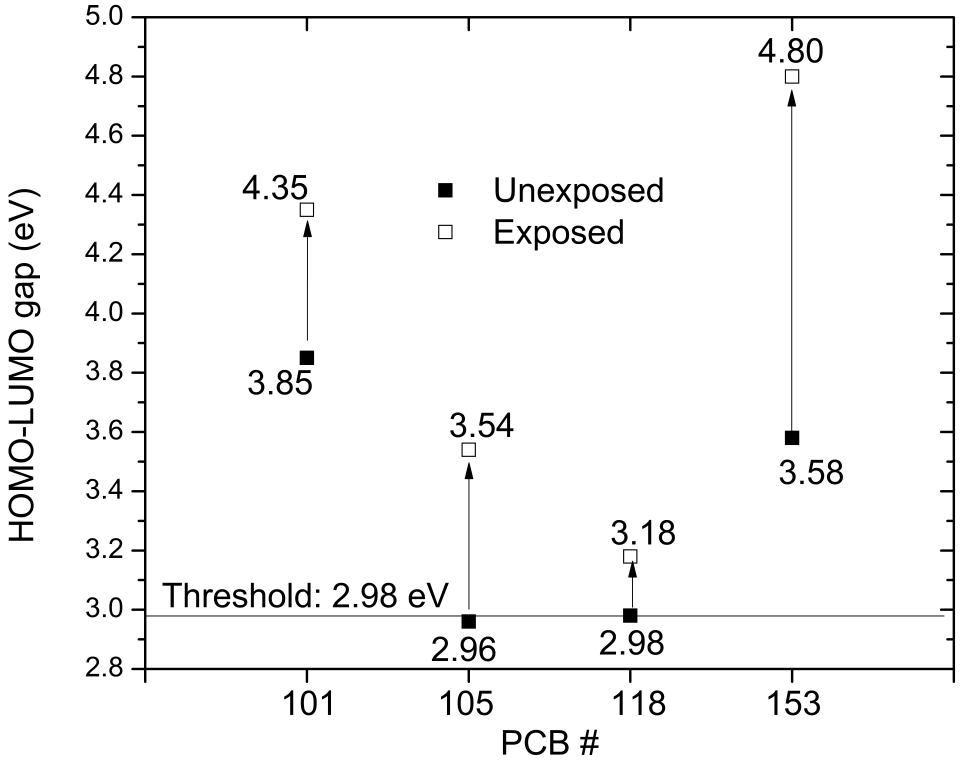

Figure 4.6: Experimental HOMO-LUMO gaps of 4 PCBs studied. The trend is for HOMO-LUMO gap to increase (toxicity to decrease) after exposure. PCB118 changes least, indicating most bio-accumulative, also indicated is an experimental HOMO-LUMO gap threshold of toxicity, similar to Fig. 4.2.

4.2 Summary

4.2.1 Toxicity Characterization of PCB Molecules

Due to the difficulties in lengthy lab tests on animals and inaccuracies in QSAR methods, we have established here a new first-principles model of the toxicity of PCBs. The first criterion for toxicity is the HOMO-LUMO gap. This divides the dioxin-like PCBs from the non-toxic ones. We then look closer at the dioxin-like PCBs and determine site activity. This activity was shown to be higher for the para- sites, secondly the meta- sites and finally the ortho- sites. We also determined that the mono-ortho PCBs have (on average) lower total activity than non-ortho PCBs. This "activity" model is consistent with established purely structural models, and in fact explains the structure models at a more physical, non-empirical level. The ranking of toxicity for the 12 dioxin-like PCBs is governed by the dipole moment direction in relation to the active para- and meta- sites. With the established model we rank the toxicity of the 12 dioxin-like PCBs. We include in our model another possible dioxin-like PCB, PCB 74, ranking it 13^{th} overall. This model does not, however convert numerically to the established TEF model, but we do not expect it to. It should be noted that even though this model only ranks the dioxin-like PCBs, which mediate through the Ah receptor, it could be adapted to investigate the relative toxicities of non-dioxin-like PCBs, and best if a test receptor is known. The model becomes most powerful when the receptor structure (particularly the DM and position of likely attachment) is known. We have also expanded this model to account for the bio-accumulation nature of PCBs. We have found that of the PCBs studied, PCB118 is the most bio-accumulative. This model, due to its first principles nature, can be expanded to other dioxin molecules. In the least it can work for other halogenated biphenyls, like poly-brominated biphenyls. Future work for validating this model can be determining the binding energy of electrons in the para-, meta- and ortho sites, as well as confirming the "threshold HOMO-LUMO gap" value with a larger sample set.

CHAPTER 5

CONCLUSIONS

Biological molecules are particularly difficult to quantify their impact on the environment without in-depth empirical studies. This thesis provided a new first-principles physical model on the toxicity of dioxin-like PCBs. The model is consistent with the accepted model, producing the same ranking as the TEF model. The first principles model is based on "site-specific activity", the partial electronic charge between a neutral molecule and an ionized molecule. This site-specific activity is the reason certain chlorination patterns are more toxic than others, particularly di-para, non-ortho PCBs. We have determined through the model that the HOMO-LUMO gap is the most important factor when considering whether a PCB is dioxin-like or not. The trend of HOMO-LUMO gap among congeners also determines the toxic-state of the family of molecules. The DFT and XAS/NXES results indicate a threshold HOMO-LUMO gap for dividing non-AhR agonist from AhR agonist PCBs, but more experimental work will need to be done to confirm that value. The model introduces another PCB into the dioxin-like family which the TEF model does not, PCB74. To confirm its place in the family, more work will need to be done on that particular congener. This model has the capability of expanding to other similar molecules, both synthetic and natural. Applications of this model include the limited use of laboratory animals and less intensive long term studies on toxicity.

REFERENCES

[1] Safe, S., *Critical Reviews in Toxicology*, **24** (1994), 87.

[2] DiGiovanni, J., Viaje, A., Berry, D., Slaga, T., and Juchau., M., *Bull. Environ. Cont. and Tox.*, **5** (1977), 522.

[3] Seegal, R., *Critical Reviews in Toxicology*, **26** (1996), 709.

[4] Birnbaum, L., *Env. Health Perp.*, **102** (1994), 676.

[5] Zimmermann, G., Dietrich, D., Schmid, P., and Schlatter, C., *Chemosphere*, **34** (1997), 1379.

[6] Lynam, M., Kuty, M., Damborsky, J., Koca, J., and Adriaens, P., *Environ. Toxicol. Chem.*, **17** (1998), 988.

[7] Quensen, J., Tiedje, J., and Boyd, S., *Science Reports*, **242** (1988), 752.

[8] Hsia, M., Lin, F., and Allen, J., *Res. Commun. Chem. Pathol. Pharmacol.*, **21** (1978), 485.

[9] Oprea, T. I., Nielsen, S. K., Ursu, O., Yang, J. J., Taboureau, O., Mathias, S. L., Kouskoumvekaki, I., Sklar, L. A., and Bologa, C. G., *Molec. Inform.*, **30** (2011), 100.

[10] Ballhausen, C. and Gray, H., *Molecular orbital theory: an introductory lecture note and reprint volume*. W.A. Benjamin, Inc., New York (1965).

[11] Hofmann, A., *Proc. Roy. Soc.*, **8** (1855), 1.

[12] Thomas, L., *Proc. Cambridge Phil. Soc.*, **23** (1927)(5), 542.

[13] Fermi, E., *Rend. Accad. Naz. Lincei*, **6** (1927), 602.

[14] Hohenberg, P. and Kohn, W., *Phys. Rev.*, **136** (1964), 864.

[15] Kohanoff, J., *Electronic Structure Calculations for Solids and Molecules*. Cambridge University Press, New York (2006).

[16] Kohn, W. and Sham, L., *Phys. Rev.*, **140** (1965), A1133.

[17] Slater, J., *Phys. Rev.*, **32** (1928), 339.

[18] Dirac, P., *Proc. Cambridge Phil. Soc.*, **26** (1930), 376.

[19] Ceperley, D. and Alder, B., *Phys. Rev. Lett.*, **45** (1980), 566.

[20] Misawa, S., *Phys. Rev.*, **140** (1965), A1645.

[21] Gell-Mann, M. and Brueckner, K., *Phys. Rev.*, **106** (1957), 364.

[22] Perdew, J. and Zunger, A., *Phys. Rev. B*, **23** (1981), 5048.

[23] Becke, A., *Phys. Rev. A*, **38** (1988), 3098.

[24] Lee, C., Yang, W., and Parr, R., *Phys. Rev. B*, **37** (1988), 785.

[25] Boys, S., *Proc. Roy. Soc. London*, **200** (1950), 542.

[26] Frisch, M. J., Trucks, G. W., Schlegel, H. B., Scuseria, G. E., Robb, M. A., Cheeseman, J. R., Montgomery, J. A., Vreven, T., Kudin, K. N., Burant, J. C., Millam, J. M., Iyengar, S. S., Tomasi, J., Barone, V., Mennucci, B., Cossi, M., Scalmani, G., Rega, N., Petersson, G. A., Nakatsuji, H., Hada, M., Ehara, M., Toyota, K., Fukuda, R., Hasegawa, J., Ishida, M., Nakajima, T., Honda, Y., Kitao, O., Nakai, H., Klene, M., Li, X., Knox, J. E., Hratchian, H. P., Cross, J. B., Bakken, V., Adamo, C., Jaramillo, J., Gomperts, R., Stratmann, R. E., Yazyev, O., Austin, A. J., Cammi, R., Pomelli, C., Ochterski, J. W., Ayala, P. Y., Morokuma, K., Voth, G. A., Salvador, P., Dannenberg, J. J., Zakrzewski, V. G., Dapprich, S., Daniels, A. D., Strain, M. C., Farkas, O., Malick, D. K., Rabuck, A. D., Raghavachari, K., Foresman, J. B., Ortiz, J. V., Cui, Q., Baboul, A. G., Clifford, S., Cioslowski, J., Stefanov, B. B., Liu, G., Liashenko, A., Piskorz, P., Komaromi, I., Martin, R. L., Fox, D. J., Keith, T., Al-Laham, M. A., Peng, C. Y., Nanayakkara, A., Challacombe, M., Gill, P. M. W., Johnson, B., Chen, W., Wong, M. W., Gonzalez, C., and Pople, J. A., Gaussian 03, revision E.01 (2004).

[27] Takeda, T., A., M., Itai, Y., Jin, W., and K., H., *Acad. Rad.*, **2** (1995), 799.

[28] Kellermann, G., Vicentin, F., Tamura, E., Rocha, M., Tolentino, H., Barbosa, A., Craievich, A., and Torriani, I., *J. Appl. Cryst.*, **30** (1997), 880.

[29] Koningsberger, D. and Prins, R., *X-ray absorption: Principles, applications, techniques of EXAFS, SEXAFS and XANES*. John Wiley and Sons, Inc., New York (1987).

[30] Synchrotron light. www.lightsource.ca/education/pdf/materials/1.3_Synchrotron_Light.pdf (2012).

[31] Synchrotron. en.wikipedia.org/wiki/Synchrotron (2012).

[32] Griffiths, D. J., *Introduction to Electrodynamics*. Prentice Hall of India, 3rd ed. (2007).

[33] Jackson, J. D., *Classical Electrodynamics Third Edition*. Wiley, 3rd ed. (1998).

[34] High resolution and flux for materials and surface science: Beamline 8.0.1. www.als.lbl.gov (2012).

[35] Krause, M., *J. Phys. Chem. Ref. Data*, **8** (1979), 307.

[36] Lawrence, C., *Phys. Fluids*, **31** (1988), 2786.

[37] Henke, B., Gullikson, E., and Davis, J., *At. Data Nucl. Data Tables*, **54** (1993), 181.

[38] Beetz, T. and Jacobsen, C., *J. Synchrotron Rad.*, **10** (2003), 280.

[39] Coffey, T., Urquhart, S., and Ade, H., *Electron Spect. Relat. Phenom.*, **122** (2002), 65.

[40] Weik, M., Ravelli, R., Kryger, G., McSweeney, S., Raves, M., Harel, M., Gros, P., Silman, I., Kroon, J., and Sussman, J., *Proc. Nat. Acad. Scie.*, **97** (2000)(2), 623.

[41] Achkar, A., *Inverse Partial Fluorescence Yield Spectroscopy*. Master's thesis, University of Waterloo (2011).

[42] Regier, T., Krochak, J., Sham, T., , Hu, Y., Thompson, J., and Blyth, R., *Nucl. Instrum. Methods Phys. Res., Sect. A*, **582** (2007), 93.

[43] Jia, J., Calcott, T., Yurkas, J., Ellis, A., Himpsel, F., Samant, M., St$'$or, J., Ederer, D., Carlisle, J., Hudson, E., Terminello, L., Shuh, D., and Perera, R., *Rev. Sci. Instrum.*, **66** (1995), 1394.

[44] Van den Berg, M., Birbaum, L., Denison, M., De Vito, M., Farland, W., Feeley, M., Fiedler, H., Hakansson, H., Hanberg, A., Haws, L., Rose, M., Safe, S., Schrenk, D., Tohyama, C., Tritscher, A., Tuomisto, J., Tysklind, M., Walker, N., and Peterson, R., *Tox. Sci.*, **93** (2006), 223.

[45] Chana, A., Concejero, M., de Frutos, M., Gonzalez, M., and Herradon, B., *Chem. Res. Tox.*, **15** (2002), 1514.

[46] Bazylewski, P., Kim, K., Forrest, J., Tada, H., Choi, D., and Chang, G., *Chem. Phys. Lett.*, **90** (2011), 508.

Appendix A Proofs

A.1 $H_{AB} < 0$

From Sec. 2.1, H_{AB} is not obviously negative. Calling $H_{AB}/H_{AA} = \zeta$, from Eq. 2.14,

$$E = H_{AA}\left[\frac{1 \pm \zeta}{1 \pm S}\right] \tag{A.1}$$

The final energy of the system (E) will be less than H_{AA} otherwise the system will not bond, therefore

$$\frac{1 \pm \zeta}{1 \pm S} > 1 \tag{A.2}$$

or

$$\pm\zeta > \pm S \tag{A.3}$$

Since S is positive by definition and H_{AA} is negative by convention, then by Eq. A.3, H_{AB} must be negative.